Master's Thesis
Master's Programme in Atmospheric Sciences
Physics/Aerosol Physics

Fragmentation patterns of particulate organic nitrates in an Aerosol Mass Spectrometer

Frans Graeffe

November 6, 2019

Supervisors: Assoc. Prof. Mikael Ehn, MSc Liine Heikkinen

Examiners: Assoc. Prof. Mikael Ehn, Prof. Tuukka Petäjä

University of Helsinki
Faculty of Science

PL 64 (Gustaf Hällströmin katu 2a)
00014 Helsingin yliopisto

HELSINGIN YLIOPISTO — HELSINGFORS UNIVERSITET — UNIVERSITY OF HELSINKI

Tiedekunta — Fakultet — Faculty	Koulutusohjelma — Utbildningsprogram — Degree programme
Faculty of Science	Master's Programme in Atmospheric Sciences Physics/Aerosol Physics

Tekijä — Författare — Author

Frans Graeffe

Työn nimi — Arbetets titel — Title

Fragmentation patterns of particulate organic nitrates in an Aerosol Mass Spectrometer

Työn laji — Arbetets art — Level	Aika — Datum — Month and year	Sivumäärä — Sidantal — Number of pages
Master's Thesis	November 6, 2019	53

Tiivistelmä — Referat — Abstract

Atmospheric aerosols affect the Earth's radiative balance, visibility and human health. Therefore the formation processes and growth of these particles are important and should be studied to understand how human and natural processes affects these processes. One poorly understood and relatively little studied part of aerosols is particulate organic nitrates (pONs). These pONs are mostly formed during nighttime when NO_x, mainly emitted from fossil fuel combustion and industrial processes, and volatile organic compounds (VOCs), from both natural and anthropogenic sources, reacts in the atmosphere. The quantification of these pONs is still hard due to instrumental restrictions, although much improvement has happened during recent years. One main reason for these challenges is the difficulty to separate inorganic nitrates from organic nitrates with real-time instruments.

During this work, we generated pure pON in well controlled laboratory conditions and sampled it with an Aerosol Mass Spectrometer (AMS), an instrument widely used for measuring the chemical composition of atmospheric aerosols. We used four different pON precursors to generate pON. I investigated the fragmentation patterns of pON detected by the AMS, utilizing the high resolution of the newest model of the AMS. As older versions of the AMS has difficulties to separate nitrate-containing organic fragments due to lower resolution than the AMS I used, I was able to study pON mass spectrum with better resolution than anyone before me. I found mass spectral differences for the different pON precursors, and was able to find unique fragments for some of the pON precursors that possibly can be used as marker fragments.

Avainsanat — Nyckelord — Keywords

AMS, pON, fragmentation patterns

Säilytyspaikka — Förvaringsställe — Where deposited

E-thesis, University of Helsinki

Muita tietoja — Övriga uppgifter — Additional information

Contents

1. Introduction

Atmospheric aerosols are small solid or liquid particles suspended in air affecting Earth's radiative balance [Russell et al., 1999] and visibility [Charlson, 1969] [Lee et al., 2017]. In addition, they affect negatively on human health [Pöschl, 2005]. Aerosols are emitted either directly to the atmosphere, for example as anthropogenic soot particles from fossil fuel combustion or naturally from oceans as sea salt particles and pollen from vegetation, or are formed secondarily in the atmosphere from condensing vapours. The size, shape, chemical composition, electrical charge and other physical and chemical properties affect how the aerosol particle will interact with its surrounding.

Aerosol particles, ranging in size from a few nm to $\sim$ 100 µm, are often measured in number and mass concentration. Even in clean and remote locations (Pallas, Finland), the atmosphere can contain up to 1000 particles per cubic centimeter (cm^{-3}) [Laakso et al., 2003] and in highly polluted urban environments (e.g. New Delhi, India) it can be as high as 200000 cm^{-3} [Mönkkönen et al., 2004]. The mass concentration has also a wide range, and in the New Delhi study it was as high as 671 µg m^{-3}. Extremely low particle number concentrations, lower than 1 cm^{-3}, has been measured in operating rooms in hospitals [Li and Hou, 2003].

In both low and high number concentrations, aerosol particles effect Earth's radiative balance either directly or indirectly. The direct effect is absorption and reflection of solar radiation; dark soot and ash particles absorbs more radiation and warms up the atmosphere while lighter particles scatter solar radiation back to space. Indirect effects come from clouds as all cloud droplets are formed on an aerosol particle, and the aerosol particles' properties will affect the cloud droplets formation and lifetime [Lohmann and Feichter, 2005]. Further, these cloud droplets scatter and absorb solar radiation, affecting the climate. In addition, scattering from aerosol particles affect visibility; higher particle concentration leads to worse visibility. High number and mass concentration, also depending on their chemical composition, is associated with several health issues, including lung and cardiovascular diseases and increased mortality [Brook, 2008] [Abbey et al., 1999] [Lelieveld et al., 2015].

As earlier mentioned, aerosols affect the atmosphere and humans in sev-

eral ways and therefore it is important to understand how different conditions affect aerosol formation. Ever since the industrial revolution in the late 18th century, anthropogenic emissions, especially from fossil fuel combustion, have changed, and still changes, the atmospheres composition [Horowitz and Jacob, 1999][Wuebbles and Jain, 2001][Dignon, 1992] and therefore affect the aerosol formation processes. Several aerosol formation processes are known and well understood, especially the inorganic aerosol formation. The processes to produce organic aerosols are more complex than the inorganics, and not all the processes and their contribution to the total aerosol formation are known.

An example of an aerosol formation process where natural and anthropogenic emissions interacts and produces aerosols is the formation of particulate organic nitrates (pON). pON can form from biogenic (or anthropogenic) emissions and NO_x ($NO + NO_2$), mostly emitted from fossil fuel combustion and industrial processes. As NO_x also is an air pollutant, leading to cardiovascular and respiratory diseases [Chaloulakou et al., 2008], the atmospheric NO_x cycle is important to understand. Further, the formation of pON is a sink for NO_x, and understanding the whole NO_x and pON cycle is essential for air quality control.

The focus in this work is the detection of pON and its separation from inorganic nitrate aerosols via mass spectrometry. This is achieved by investigating the fragmentation patterns of pON from several pON precursors in an Aerosol Mass Spectrometer (AMS), an instrument widely used for measuring the chemical composition of atmospheric aerosols. Unlike previous studies where an AMS has been used, I utilized the newest model of the AMS with its higher resolution to investigate pON-fragments in more detail than earlier possible.

2. Theory

2.1 Atmospheric aerosols

Atmospheric aerosols are either emitted directly through different sources or secondarily formed in the atmosphere. Sea salt, dust, pollen and ash are examples of primary aerosols while secondary aerosols are formed in the atmosphere via gas to particle conversion. Secondary aerosols can form via inorganic or organic precursors, or a combination of them. The formation of particle phase ammonium (NH_4^+), sulfate (SO_4^{2-}) and nitrate (NO_3^-) from the inorganic gases ammonia (NH_3), sulfur dioxide (SO_2), nitrogen dioxide (NO_2) is fairly well understood. However, the aerosol formation from organic compounds introduces a large uncertainty in the knowledge of their formation mechanisms, properties and composition. As there are estimately up to 100000 measured organic compounds in the atmosphere [Goldstein and Galbally, 2007], the complexity of organic aerosols is enormous.

In this work, the emphasis is on the detection of particulate organic nitrates (pON) and its separation from inorganic nitrates via mass spectrometry. Therefore, the following subsections emphasize the formation of both inorganic and organic nitrates, including the NO_x cycle and volatile organic compounds (VOCs), without going into detail on other aerosol formation processes.

2.1.1 Inorganic nitrate aerosol

The most commonly measured inorganic aerosol species are ammonium sulfate and ammonium nitrate. Here, we present the formation of ammonium nitrate and other, less common, nitrate salts.

2.1.1.1 Ammonium nitrate

Atmospheric ammonium nitrate (NH_4NO_3, AN) is a product of ammonia (NH_3) and nitric acid (HNO_3):

$$NH_3(g) + HNO_3(g) \rightarrow NH_4NO_3(s) \tag{2.1}$$

The main sources of ammonia are anthropogenic emissions [Bouwman et al., 1997]; mainly from agricultural activities, for example fertilizers and domestic animals, although in urban areas, traffic emissions can also be a significant source of ammonia [Phan et al., 2013]. The ammonia emissions have been increasing, and are predicted to increase in the future [Bouwman et al., 1997] [Warner et al., 2017]. Nitric acid is primarily formed, during daytime, when NO_2 reacts with the OH radical:

$$NO_2 + OH \rightarrow HNO_3 \tag{2.2}$$

2.1.1.2 Other inorganic nitrate salts

Other, less common, inorganic nitrate salts, like $NaNO_3$ and $Ca(NO_3)_2$ are detected at coastal sites [Allan et al., 2004]. At these sites, sea salt components like sodium chloride (NaCl) and calcium chloride ($CaCl_2$) can react with nitric acid and form these inorganic nitrate salts.

2.1.2 Organic aerosol

Primary organic aerosols (POAs) are emitted both from natural and anthropogenic sources, for example from vegetation as pollen or from vehicles during fossil fuel combustion. Secondary organic aerosol (SOA) is mainly formed via gas to particle conversion from condensable vapours; volatile organic compounds (VOCs) are oxidized and getting low enough vapour pressure to be able to condense and be part of SOA formation and growth. The vast amount of SOA precursors and formation pathways leads to complex chemical composition of SOA. Therefore, it is really hard to chemically identify or separate all the compounds, even with modern measurement techniques. Additional difficulty to detection is introduced by particle phase reactions.

Several oxidation processes for VOCs are known, but in this work we only discuss the organic nitrate formation via VOC oxidation by the nitrate radical. Thereby, the next sections discuss in more detail VOCs and the formation of the nitrate radical.

2.1.2.1 Volatile Organic Compounds (VOCs)

A VOC is an organic gas phase compound that has an effective saturation concentration, C^* (describing the volatility of an compound), larger than $3 \cdot 10^6$ µg m^{-3}

[Donahue et al., 2012]. Carbon monoxide (CO) and carbon dioxide (CO_2) are not VOCs. If methane is also excluded, 90% of the VOCs are emitted from biogenic and 10% from anthropogenic sources [Seinfeld and Pandis, 2016]. Globally, the largest non-methane biogenic VOC (BVOC), emitted from the vegetation, measured in mass concentration, is isoprene (C_5H_8) ($\sim$ 70%), followed by monoterpenes ($C_{10}H_{16}$) ($\sim$ 11%) [Sindelarova et al., 2014]. To monoterpenes belongs for example α-pinene, β-pinene and limonene, and they are the major BVOCs in the boreal forest in the northern hemisphere [Rinne et al., 2009]. Anthropogenic VOCs are mainly alkanes, aromatics and alcohols emitted for example from combustion processes and solvents [Theloke and Friedrich, 2007].

When emitted to the atmosphere, VOC are primarily oxidized by ozone (O_3), the hydroxyl radical (OH) and nitrate radical (NO_3). VOCs can be oxidized several times, lowering their volatility until they condense and form SOA. During daytime, OH radical is the dominant oxidant, while during night-time the NO_3 radical plays a major role.

The VOCs used in this work are presented in more detail later on in Section 4.1.2.

2.1.2.2 NO_x and NO_3 chemistry

The main sources of tropospheric NO_x ($NO_x = NO + NO_2$) are fossil fuel combustion and industrial processes [Seinfeld and Pandis, 2016], contributing nearly 60% of the total NO_x emissions. Natural sources, like soils and lightnings, accounts for 23% of the total NO_x emissions. The NO_x chemistry differs a lot during day- and nighttime. During daytime, NO is rapidly oxidized by ozone (O_3) to NO_2 and NO_2 is photolysed back to NO. During nighttime, when no sunlight is present, NO is converted to NO_2 by:

$$NO + O_3 \rightarrow NO_2 + O_2 \tag{2.3}$$

Further, the nitrate radical (NO_3) is produced from NO_2 oxidation by O_3:

$$NO_2 + O_3 \rightarrow NO_3 + O_2 \tag{2.4}$$

Reaction 2.4 is the only direct atmospheric source of NO_3, an indirect source is through thermal decomposition of N_2O_5:

$$N_2O_5 + M \leftrightarrow NO_2 + NO_3 + M \tag{2.5}$$

Reaction 2.5 reaches an equilibrium within a few minutes [Seinfeld and Pandis, 2016] during nighttime. During daytime, any nitrate radicals would decompose either via photolysis or via reaction with NO within seconds:

$$NO_3 + \lambda(< 700\text{nm}) \rightarrow NO + O_2 \tag{2.6}$$

$$NO_3 + \lambda(< 580\text{nm}) \rightarrow NO_2 + O \tag{2.7}$$

$$NO_3 + NO \rightarrow 2NO_2 \tag{2.8}$$

Hence, the nitrate radical is important mainly during nighttime chemistry as it is a strong oxidant for a wide range of VOCs. Especially fast reactions with NO_3 occurs with unsaturated compounds (containing at least one carbon-carbon double or triple bond) [Atkinson and Arey, 2003], for instance alkenes. The low volatility compounds formed during oxidation of BVOCs by the NO_3 radical, producing SOA, is a direct link between biogenic carbon in atmospheric aerosols and anthropogenic pollution (NO_x).

2.1.2.3 Particulate organic nitrate (pON)

Although it is known that organic aerosols are a major part of atmospheric aerosols, there are still large uncertainties related to the sources of these organic compounds [Hallquist et al., 2009]. Modelling studies [Spracklen et al., 2011] show that reactions between anthropogenic emissions and BVOCs could play an important role in the global SOA budget. One candidate for the source of this organic mass is particulate organic nitrate (pON). For example, [Kiendler-Scharr et al., 2016] presented results from measurements around Europe, during several seasons, that pON could account for up to 44% of the submicron nitrate aerosol. In addition, [Lee et al., 2016] estimated that pON could account for 8% of the total nighttime OA mass in the south-east Unites States.

Organic nitrates, in the gas phase, are formed by oxidation of VOCs by NO_3 radicals, adding a nitrate (-ONO_2) functional group to the VOC and lowering their vapour pressure. Further, pON is formed when organic nitrates in the gas phase are partitioning to the particulate phase and form SOA.

2.2 Challenges in aerosol measurements

Besides the vast chemical complexity for organic aerosols, another major reason for difficulties in chemical characterization of aerosols is the wide range of sizes. A particle with a diameter of 1 nm and 1 µm will have a mass of approximately 10^{-21} g (zeptograms) and approximately 10^{-12} g (picograms), respectively. In atmospheric studies,

the time-dependent evolution of the aerosol particles is often an aspect of interest, favoring real-time instruments that do not separately collect, store and analyze the samples.

For particulate organic nitrates (pON) there is yet no accurate real-time analysis method to detect pON and quantify them. Off-line methods can give more specific information of the chemical composition and structure, while real-time instruments usually gain the time-resolution by giving up the chemical specificity.

In this work, we used an Aerosol Mass Spectrometer (AMS) designed and developed by Aerodyne Research, Inc. (ARI). The AMS is a real-time instrument that can measure size-resolved chemical composition of non-refractory submicron particles from ambient pressure (for more detailed description, see Section 3.1). The AMS uses thermal vaporization and election impact ionization (70 eV) to maximize the range of detected aerosol species, but loses, via fragmentation of the original molecules, a lot of chemical information due to this hard ionization method. Most of the organic and inorganic nitrates fragment into NO^+ and NO_2^+ within the AMS. Furthermore, the ratio of NO^+ and NO_2^+ (NO_x^+ ratio) differs depending if the nitrate comes from organic or inorganic compounds, and this could potentially be used to quantify pON from ambient data [Farmer et al., 2010] by

$$x = \frac{(R_{\text{obs}} - R_{\text{AN}})(1 + R_{\text{pON}})}{(R_{\text{pON}} - R_{\text{AN}})(1 + R_{\text{obs}})} \tag{2.9}$$

Where x is the fraction of the total nitrate signal due to organic nitrates. R is the NO_x^+ ratio for ammonium nitrate (AN), particulate organic nitrate (pON) and the ambient observed ratio (obs).

The main source of inorganic nitrate in the atmosphere is ammonium nitrate, except at coastal sites where $NaNO_3$ and $Ca(NO_3)_2$ can contribute significantly to the inorganic nitrate portion, increasing the NO_x^+-ratio [Allan et al., 2004]. Several studies has shown that the NO_x^+ ratio for pure AN is ranging from 1 to 3 while it is way higher for pON, ranging often from 5 to 10 (see Figure 5.10 for ratios from previous studies).

There are still several problems for using the NO_x^+ ratio for pON quantification. First, the NO_x^+ ratio for pON differs a lot depending on the precursors available on different sites and different precursors give different NO_x^+ ratios. Additional uncertainty is also introduced by an organic fragment, CH_2O^+, which is often present in ambient measurements at the same unit mass as the NO^+ fragment. If the resolution of the instrument is not good enough to separate these two fragments, underestimation of the organic fragment can lead to significant overestimation of pON. If the pON concentrations are too low, this approach is not capable of quantifying pON, restricting this method to locations with large fraction of pON. Additionally, this method does

not work at costal sites where $NaNO_3$ or $Ca(NO_3)_2$ are present.

3. Instruments

In this section, the working principles of the three main instruments (AMS, PAM, AAC) for this work is presented in more detail, while other instruments are described shortly in the methods section when mentioned.

3.1 Aerosol Mass Spectrometer (AMS)

The Time of Flight Aerosol Mass Spectrometer (ToF-AMS) is a real-time instrument that can measure size-resolved chemical composition of submicron particles from ambient pressure. The working principles of a Long-ToF-AMS (L-ToF-AMS), the main instrument in this work, is similar to the High Resolution (HR) ToF-AMS (DeCarlo et al. 2006), but it is mounted with a longer ToF-chamber enabling over two times higher resolution. There are different versions of the AMS (described in Section 3.1.5); all of them are based almost on the same techniques, but some differences related to technique development and achieving desired functionalities are found. The four main parts of the AMS are 1) the aerosol inlet, where the sampling takes place, 2) the particle sizing chamber, where the size of the particles are measured, 3) the vaporisation and ionisation chamber, where the solid or liquid particles are vaporised and ionised and 4) mass analyser, where the chemical composition of the particles are measured via mass spectrometry (quadrupole or time-of-flight mass analysers). The AMS is developed and manufactured by Aerodyne Research Inc., Billerica, Massachusetts, United States.

The schematics of the L-ToF-AMS is shown in Figure 3.1

3.1.1 Inlet and aerodynamic lens

The AMS samples air through a critical orifice (diameter = 100 µm), which drops the pressure from ambient (101.325 kPa) to under 300 Pa [Canagaratna et al., 2007]. The flow is now led through an aerodynamic lens system, which focuses the particles to a narrow beam with a diameter of approximately 1 mm. The transmission efficiency of the aerodynamic lens is a function of particle diameter, and has been studied both experimentally and theoretically for example by [Liu et al., 2007]. Depending on the

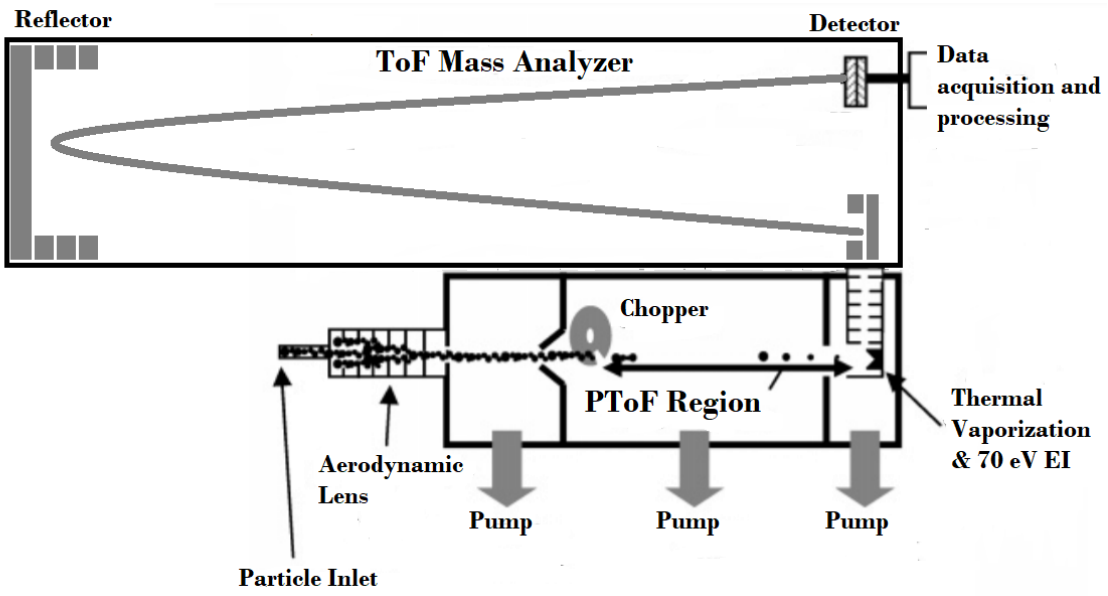

Figure 3.1: The schematics of the L-ToF-AMS (Figure from [DeCarlo et al., 2006], modified from the HR-ToF-AMS schematic)

definition of transmission, the AMS is reported to detect particles with an aerodynamic diameter between 40 nm and 1 µm. Particle trajectories inside the lens system is shown in Figure 3.2.

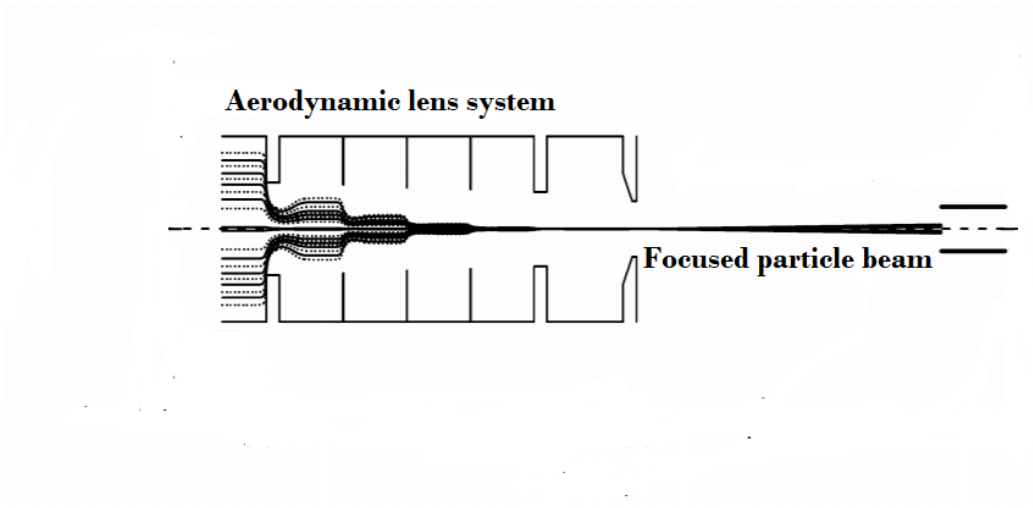

Figure 3.2: Particle trajectories inside the aerodynamic lens, focusing the particles to a narrow beam (figure from Zhang et al. 2004, modified)

3.1.2 Particle sizing chamber

When exiting the aerodynamic lens, and entering the sizing region of the instrument, the flow undergoes a supersonic expansion where the particles are accelerating and

achieving a velocity-distribution depending on their aerodynamic size. The particle size is calculated from the particle time of flight (PToF) across a well-defined distance ($\sim$ 30 cm) between a chopper and the ionization chamber (PToF region). The beginning of the flight time starts at a mechanical chopper, mounted after the aerodynamic lens and consisting of 32 slits on the chopper wheel ($\sim$ 5 cm in diameter, see Figure 3.3), chopping the particle beam with a 90 Hz frequency. The particle flight time ends at the mass spectrometric detection providing chemically resolved particle size-data, although the PToF region ends before it. This is possible because the particle flight time is on the millisecond scale ($\sim$ 3 ms) and the vaporization, ionization and MS-detection is on the microsecond scale ($\sim$ 50 µs). The original PToF chopper had only 1 slit (instead of 32 slits) chopping the particle beam, but newer models of the AMS uses this chopper with 32 slits and is called efficient particle time of flight (ePToF). The ePToF, utilizing a Hadamard trasform [Zare et al., 2003], reaches higher transmission ($\sim$ 50%) of particles compared to the old PToF version that had only $\sim$ 2% transmission. The AMS used in this work was equipped with the ePToF chopper.

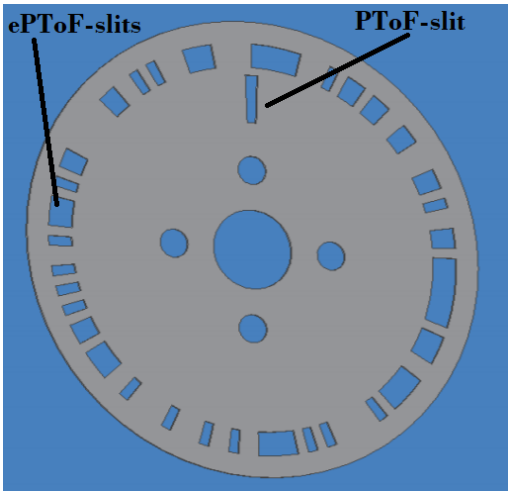

Figure 3.3: Chopper from AMS particle sizing chamber. The one inner slit (PToF-slit) is used for PToF-mode and all of the outer slits (ePToF-slits) are used to chop the particle beam during ePToF-mode. The one big circular hole and the four smaller in the middle are used for mounting the chopper to the axis that moves the chopper between the different modes (Figure from [Aerodyne,], modified)

Besides the particle sizing measurements, the chopper has another very important function. It is used to measure the background signal from the air that has not been removed from the chamber by the pumps. The chopper has four different modes that can be used during measurements: open, closed, PToF and ePToF. In open-mode, the chopper is moved away from the particle beam, allowing all particles and air to reach the vaporisation and ionisation chamber. In closed-mode, the chopper is blocking all particles and used to calculate the signal obtained from the ionised background gases.

The difference of open- and closed-mode is used as the signal from the sampled aerosols. PToF and ePToF is used as earlier described. Usually, the AMS is operated by altering the open/closed-modes and ePToF (or PToF) with different frequencies, depending on wanted amount of particle size and chemical composition data.

For this work, no ePToF data were analyzed because we selected well-defined monodisperse aerosols with an AAC (described later on in Section 3.2) before sampling it with the AMS.

3.1.3 Vaporisation and ionisation

After the PToF region, the particles enters the vaporization and ionization chamber where they are flash vaporised by impact on an $\sim$ 600℃ porous tungsten surface. The vaporizer has a diameter of $\sim$ 4 mm and is formed as an inverted cone to reduce unwanted particle bounce that reduces the collection efficiency of particles [Middlebrook et al., 2012]. Due to the selected vaporisation method only "non-refractory" (NR) species are vaporised (defined as those species that are vaporised in these condition), including organics and most nitrate and sulfate salts. This means that sea salt, metals and black carbon are not detected by the AMS [Canagaratna et al., 2007]. The gaseous molecules are now ionised through electron ionisation (EI, formerly referred as electron impact ionisation). Schematics of the vaporisation and ionisation chamber is shown in Figure 3.4. EI is based on shooting energetic electrons (70 eV in the AMS) on neutral vapors and transferring some of the kinetic energy to the sample molecules when colliding. If the collision is successful, the transferred energy exceeds the ionisation energy of the molecule and the molecule loses an electron and forms a molecular ion (a positive radical ion):

$$M + e^- \rightarrow M^+ + 2e^-$$

EI is an easy ionisation method with good repeatability and it is non-selective, ionizing both organics and inorganics. As the AMS uses standard 70 eV EI, its mass spectra can be compared to the National Institute of Standards and Technology (NIST) mass spectral database [Linstrom and Mallard, 2001] and an intercomparison of AMS and NIST spectra from several chemical species shows that the mass spectra are very similar except from some small differences for long-chained organics [Alfarra, 2004]. The electron used in EI are generated by thermionic emission from a tungsten wire (filament), which is resistively heated up to $\sim$ 2000℃ . Extracted electrons are then accelerated by a voltage to achieve wanted 70 eV electrons. However, if the accelerated electrons have lower or higher energy than 70 eV, it may result in different fragmentation and loss of resolution and mass accuracy [Gross, 2004]. The downside of EI is the fragmentation

of the parent molecule, losing some chemical information of them. Furthermore, identification of the original molecule structure is not possible due to no prior separation method, only giving the chemical composition of the fragments. In addition, due to the large scale of possible compounds in the aerosol particle, especially organics, the detected mass spectra is a mixture of fragments from all molecules and makes it practically impossible to identify the chemical composition of any specific molecules from ambient aerosols. The fragmentation can, however, be used to identify some species if they have a specific fragmentation pattern. For example, the nitrates in both organic nitrates and inorganic nitrates fragments mostly to NO^+ and NO_2^+, but the ratio of these (the NO^+/NO_2^+-ratio, hereafter NO_x^+ ratio) is different for organic and inorganic nitrates and can be utilized for quantification of organic nitrates [Farmer et al., 2010]. More of the NO_x^+ ratio previously Section 2.2.

The detection scheme and calibration method of the AMS allows quantitative detection of ambient aerosol [Jimenez et al., 2003]. The AMS is usually calibrated with NH_4NO_3 and $(NH_4)_2SO_4$, mainly because nitrate and sulfate is common aerosol species and vaporises easily in the vaporiser.

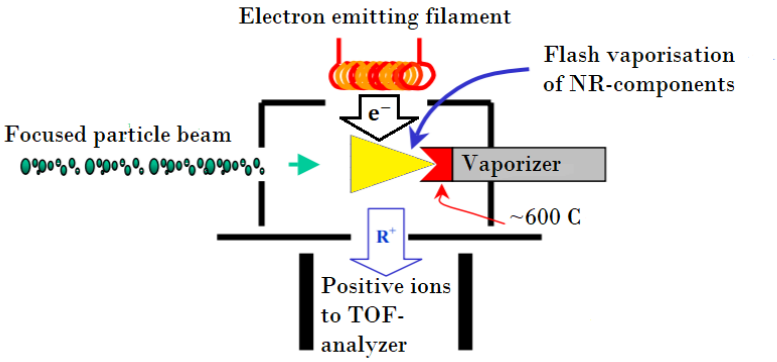

Figure 3.4: Vaporisation and ionisation chamber. Particles first hit the 600°C porous tungsten vaporiser and are then ionised by 70 eV electrons emitted from a filament. Positive ions are then directed to the ToF mass analyser (Figure from [Canagaratna et al., 2007], modified)

3.1.4 Mass analyser

The mass analyser used in most AMS versions are different length of orthogonal acceleration reflector time of flight-analysers (oaReToF, hereafter simply ToF). The basic principle for a ToF is simple: ions with different mass to charge ratio (m/z) and same initial kinetic energy, moves with different velocities in vacuum, and by knowing the length of the flight path, it is possible to calculate the m/z for the detected ions. We assume a particle at rest with the mass m and the charge q (which is equal to an integer

number z of elemental charges$e$, $q = ez$). Before entering the ToF chamber, the ions are given kinetic energy by moving through a voltage U and the energy uptake there (E_{el}) is converted to kinetic energy (E_{kin}):

$$E_{\text{el}} = qU = ezU = \frac{1}{2}mv^2 = E_{\text{kin}} \tag{3.1}$$

The ions have now the following velocity:

$$v = \sqrt{\frac{2ezU}{m}} \tag{3.2}$$

and their flight time along a field free distance L is:

$$t = \frac{L}{v} = \frac{L}{\sqrt{\frac{2ezU}{m}}} \tag{3.3}$$

Each instrument has their well-defined values for U and L, and by measuring the flight time t, the ratio m/z is:

$$\frac{m}{z} = \frac{2eUt^2}{L^2} \tag{3.4}$$

The reflectors working principle is following: behind the field-free region a retarding electric field is located and works as a mirror that changes the ions flight direction and lengthens the flight path. Differences in the initial energy for ions with same m/z-ratio, resulting in different flight time, is corrected by the reflector and increasing the resolution remarkably. This is achieved by the retarding electric field: ions with higher kinetic energy will penetrate deeper into the electric field than ions with lower energy and thus spend more time in the electric field and thereby correcting the flight time. In all AMS-versions, exluding the HR-ToF-AMS, V-mode stands for normal one-reflector mode but int the HR-ToF-AMS there is also a W-mode. In the W-mode, the ions exiting the reflector are sent back to the reflector one more time by a hard mirror (instead of going to the detector), lengthening the flight path further. The W-mode has higher resolution than V-mode, but the V-mode is more sensitive because more ions are lost in the W-mode due to lateral broadening and fewer ions reaching the detector.

In an orthogonal acceleration ToF, pulses of ions are extracted orthogonally to the ToF from the ion beam. The main advantages of oaToF is high sensitivity, high acquisition rate and compact design [Gross, 2004]. The flight path of the ions inside the ToF is seen in Figure 3.1.

In this work, no data acquisition or processing nor ion detection details are presented but can be found from [DeCarlo et al., 2006] [Sueper and collaborators,].

3.1.5 Different AMS versions

There have been several different versions of the AMS, and the main difference has been the length the ToF chamber. However, the first AMS, the Q-AMS, had a quadrupole instead of ToF chamber as mass analyser and had only unit mass resolution (UMR). Its time resolution were also significantly worse. AMS versions using a ToF, there are different versions (listed with increasing resolution): the compact (C-ToF), HR-ToF and L-ToF AMS. In the HR-ToF-AMS, there are the V- and W-mode for further increase of resolution. In Figure 3.5, the resolution a HR-ToF-AMS (V- and W-mode), a L-ToF-AMS and a Q-AMS is compared. From that figure it is clear that the L-ToF-AMS has the highest resolution and is able of separating fragments significantly better than the HR-ToF-AMS, even in W-mode. The high resolution of the L-ToF-AMS is utilized for identifying nitrogen-containing organic fragments in this work. In addition to the different AMS versions, an Aerosol Chemical Speciation Monitor (ACSM) has been developed by Aerodyne Inc. [Ng et al., 2011]. The ACSM is basically a simpler version of the AMS, but without the particle-sizing part. While the AMS is mainly meant for shorter measurements, the ACSM is developed for long-time (years) monitoring of submicron mass concentration and chemical composition. The original ACSM uses a quadrupole mass analyser, but some newer models are equipped with a ToF analyser.

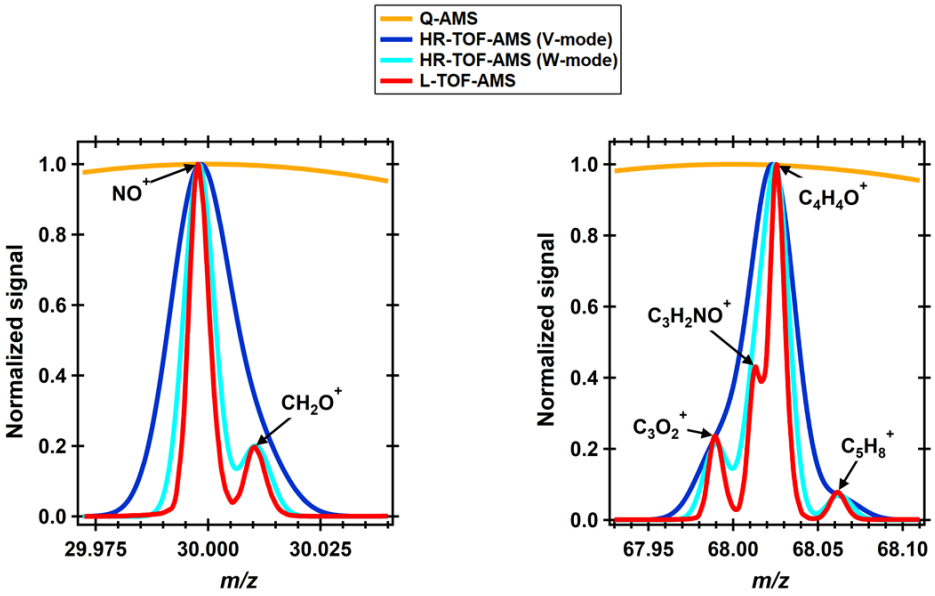

Figure 3.5: Comparison of the resolution of different AMS versions. The L-ToF-AMS data is from an actual experiment done during this work, the rest of the data is produced artificially knowing the resolution of each instrument version.

3.2 Aerodynamic Aerosol Classifier (AAC)

The aerodynamic aerosol classifier (AAC) is an instrument for selecting monodisperse aerosols from polydisperse aerosol population and it classifies aerosols according to their aerodynamic diameter [Tavakoli and Olfert, 2013]. The schematics of an AAC is shown in Figure 3.6. It consists of two concentric cylinders, rotating with same rotational speed and direction. When particles enters the AAC, from the aerosol flow (Q_{a}), they are guided through a small gap leading to a particle free sheath flow (Q_{sh}) between the two concentric cylinders. The particles experiences a centrifugal and drag force in the radial direction due to the rotating cylinders, but are also carried in the axial direction due to the sheath and aerosol flow. Particles with a specific aerodynamic diameter are now exiting the AAC with the sample flow (Q_{s}). Particles with larger aerodynamic diameter hits the inner wall before the exit and particles with smaller aerodynamic diameter hits the inner wall after the slit or exits the AAC with the exhaust flow (Q_{exh}). Particle trajectory and the flows inside the AAC is presented in Figure 3.6. The AAC is manufactured by Cambustion Ltd., Cambridge, United Kingdom.

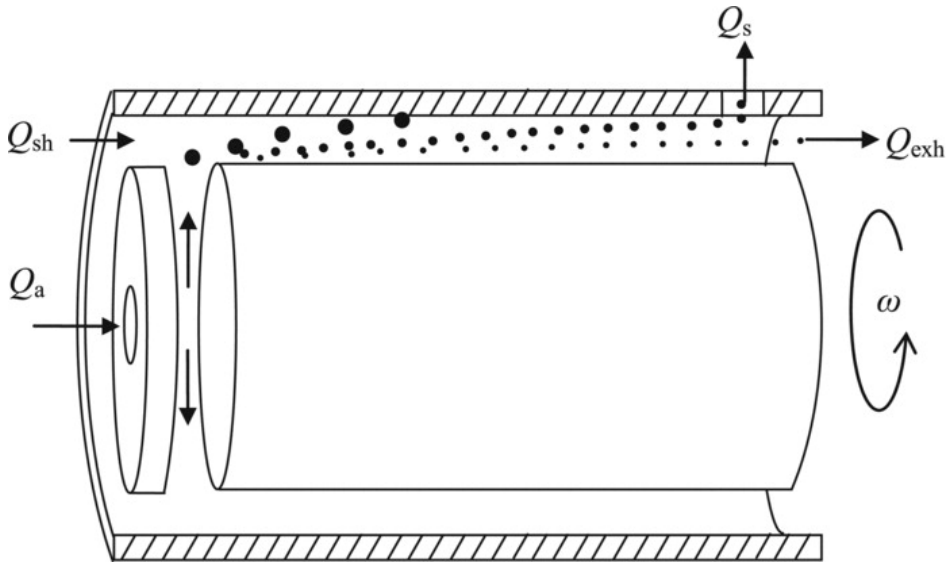

Figure 3.6: Schematics of the AAC [Tavakoli and Olfert, 2013])

3.3 Potential Aerosol Mass Oxidation Flow Reactor (PAM-OFR)

[Kang et al., 2007] defined a new concept of Potential Aerosol Mass (PAM) as the maximum aerosol mass that the oxidation of precursor gases can produce. They also

developed a small flow reactor to investigate the PAM concept. The PAM oxidation flow reactor (PAM-OFR, hereafter PAM) is a simple, small, flow-through chamber where atmospheric oxidation processes can be studied in laboratory or in field. The PAM provides a highly oxidizing environment, simulating atmospheric oxidation processes with typical atmospheric time-scales from hours up to several days in only a few minutes. The PAM is capable of shortening the typical long atmospheric oxidation-processes to only a few minutes due to extremely high amounts of oxidants introduced to the system. The PAM chamber itself is a small (13 L) cylindrical chamber, where huge amounts of oxidants (e.g O_3, OH or NO_3) and a precursor gas is introduced and then rapidly oxidized. These oxidized compounds can then form SOA that can further be investigated, for example with an AMS. Some version of the PAM has UV lamps to simulate daytime atmospheric conditions, but for this work we used a dark PAM chamber to simulate nighttime conditions and promote NO_3 radical chemistry.

4. Measurements and data analysis

4.1 Measurements

All of the measurements in this work was done during an ACSM-intercomparision at the Aerosol Chemical Monitor Calibration Centre (ACMCC) in Paris, France, during November and December 2018. During the measurements, pON was generated in a PAM from the reaction of NO_3 radicals and a VOC. We used four different pON precursor VOCs (described in Section 4.1.2) and investigated the detection and fragmentation of the generated pON in the L-ToF-AMS and ACSMs. One of the main goals during the ACSM-intercomparision was to utilize the high resolution of the L-ToF-AMS to evaluate the quantification of pON with the low-resolution ACSMs.

4.1.1 Experimental setup

The experimental setup used during the pON experiments is presented in Figure 4.1. The experimental setup was designed and set up by the ACMCC crew. The pON precursors were either introduced via a syringe pump (liquids) or a tube (powder) together with air or N_2 gas, flow rates in the lines were controlled by mass flow controllers (MFCs). The generation of nitrate radicals was done by O_3 and NO_2 reactions (Reaction 2.4 and 2.5).

Produced pON exiting the PAM was then size-selected with the AAC and monodisperse aerosols were then sampled with the L-ToF-AMS and the 8 ACSMs. The maintenance and operating of the L-ToF-AMS during the experiments was my responsibility.

4.1.2 pON precursors

We used four pON precursors (VOCs) during this experiment, two biogenic (limonene and β-pinene) and two anthropogenic (guaiacol and acenaphthylene). The chemical structure of all compounds are shown in Figure 4.2. Only acenaphthylene was introduced as powder in the system, rest of the compounds were liquids. The SOA formation

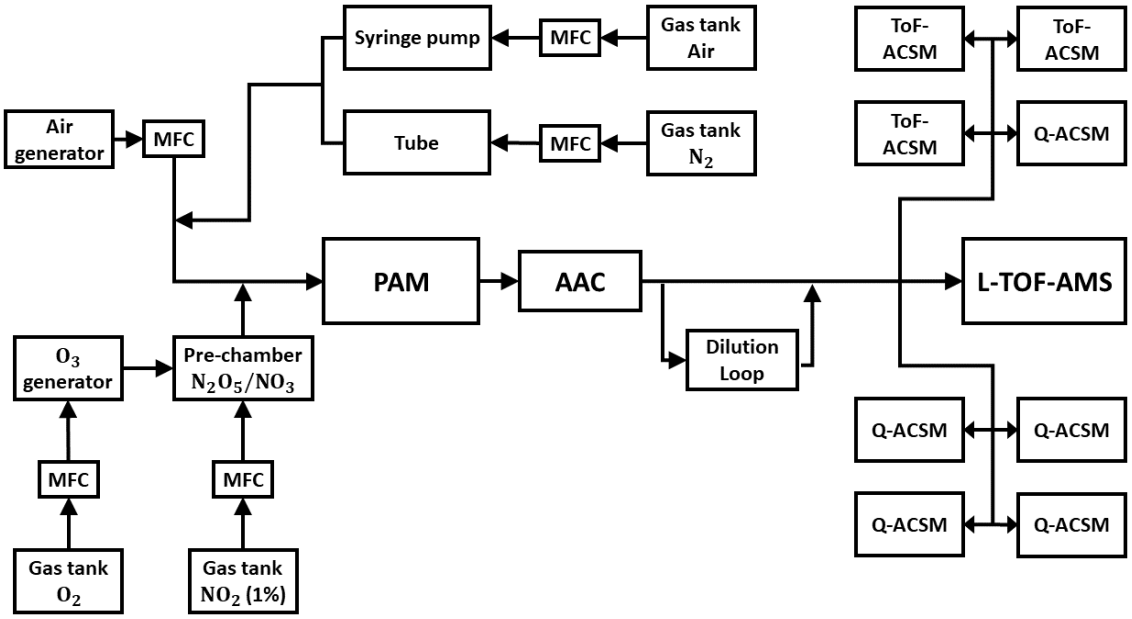

Figure 4.1: Experimental setup. pON precursors and NO_3 radicals are introduced to the PAM chamber. Before sampling the aerosols with the L-ToF-AMS and the ACSMs, monodisperse aerosol population is generated with the AAC.

in the PAM was driven by NO_3 oxidation even though some O_3 did enter the PAM, mainly because the NO_3 radicals reacts faster than O_3 with the investigated VOCs. The atmospheric lifetimes of all four precursors with respect to the three main atmospheric oxidants (NO_3, O_3 and OH) are presented in Table 4.1. From there we can easily see that the VOCs used are oxidized way faster by the nitrate radical than by O_3 in nighttime conditions and as we simulated nighttime conditions we can assume that the SOA formation in the PAM was NO_3 driven.

4.1.2.1 Guaiacol

Guaiacol (2-methoxyphenol) is a semivolatile gas phase methoxyphenol produced during biomass burning, both natural fires and human related fires such as residential wood combustion [Lauraguais et al., 2016], and can be used as a tracer for atmospheric wood smoke emissions due to its unique production from biomass burning [Hawthorne et al., 1988] [Simoneit et al., 1993].

In an oxidation flow reactor (OFR) experiment, [Liu et al., 2019] produced organic nitrates by oxidizing guaiacol with OH-radicals in presence of NO_2 and reported a NO_x^+ ratio of 4.02-6.25 detected with a HR-ToF-AMS.

Table 4.1: Atmospheric lifetimes of VOCs used in the experiments with respect to reactions with NO_3 (during nighttime), O_3 (24h average) and OH (during daytime).

Oxidant	NO_3 (nighttime)	O_3 (all day)	OH (daytime)
Acenaphthylene	7 min [a]	1 h [a]	1.3 h [a]
Guaiacol	74 s [b]	11.8 days [c]	2.3 h [b]
Limonene	9 min [d]	36 min [d]	2 h [d]
β-pinene	50 min [d]	18 h [d]	3.6 h [d]

[a] [Zhou and Wenger, 2013] $[NO_3] = 24$ ppt, $[O_3] = 280$ ppb, $[OH] = 2 \cdot 10^6 cm^{-3}$

[b] [Lauraguais et al., 2016] $[NO_3] = 20$ ppt, $[OH] = 1.6 \cdot 10^6 cm^{-3}$

[c] [Zein et al., 2015] $[O_3] = 100$ ppb

[d] [Winer et al., 1984] $[NO_3] = 10$ ppt, $[O_3] = 30$ ppb, $[OH] = 1 \cdot 10^6 cm^{-3}$

4.1.2.2 Acenaphthylene

Acenaphthylene is a polycyclic aromatic hydrocarbon (PAH) mainly emitted from fossil fuel combustion, both from liquid and solid fuels [Ravindra et al., 2008]. Under normal atmospheric conditions acenaphthylene exists in gas phase and it is highly reactive to atmospheric oxidants due to its carbon-carbon double bond.

The purity of the acenaphthylene used in this experiment was only 75%, the rest was acenaphthene that differs from acenaphthylene only by one carbon-carbon double bond less (chemical structure shown in Figure 4.2e).

4.1.2.3 Limonene

Limonene is one of the most emitted monoterpenes in the nature (Sakulyanontvittaya et al. 2008 and [Guenther et al., 2012], but it is also used in several air fresheners and cleaning products [Wainman et al., 2000] due to its lemon/citrus scent. Limonene possesses two double bonds and oxidizes rapidly in the atmosphere and can easily form products that can further form SOA. Earlier reported NO_x^+ ratios from limonene + NO_3 systems are ~ 6.67 [Fry et al., 2011] and 6.3 [Boyd et al., 2017].

4.1.2.4 β-pinene

β-pinene is a more abundantly emitted monoterpene than limonene [Guenther et al., 2012] and a modelling study from 2005 (Russel and Allen) suggested that up to 20% of nocturnal SOA is formed through β-pinene + NO_3 reactions. Beta-pinene + NO_3 systems has been frequently studied and NO_x^+ ratios from 6.3 to 10 has been reported [Fry et al., 2009], [Nah et al., 2015],[Boyd et al., 2015], [Boyd et al., 2017].

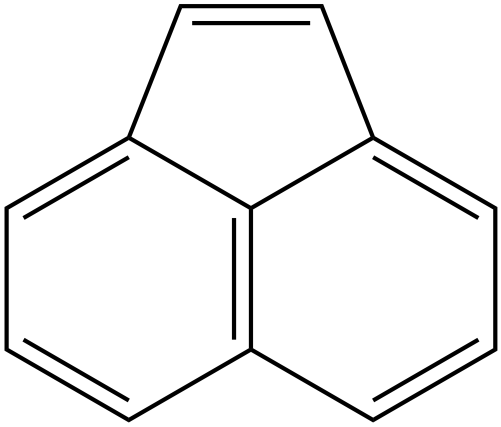

(a) Acenaphthylene

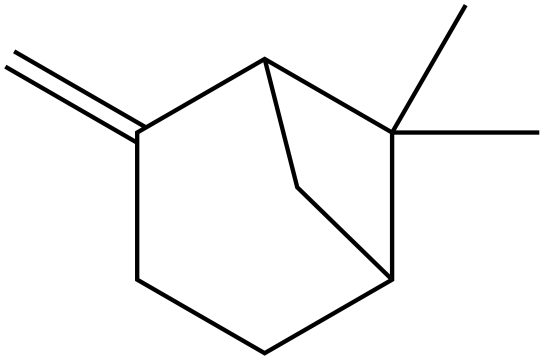

(b) β-pinene

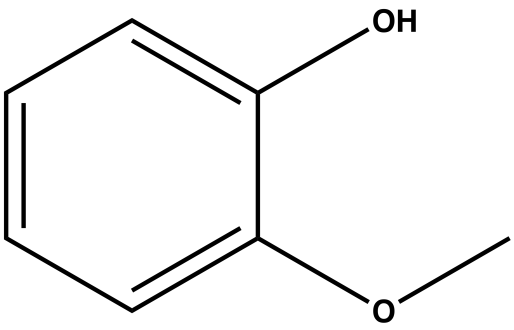

(c) Guaiacol

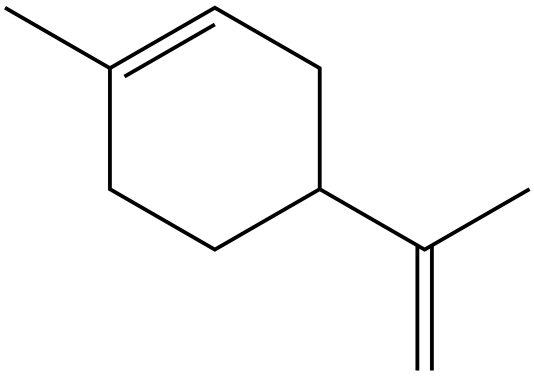

(d) Limonene

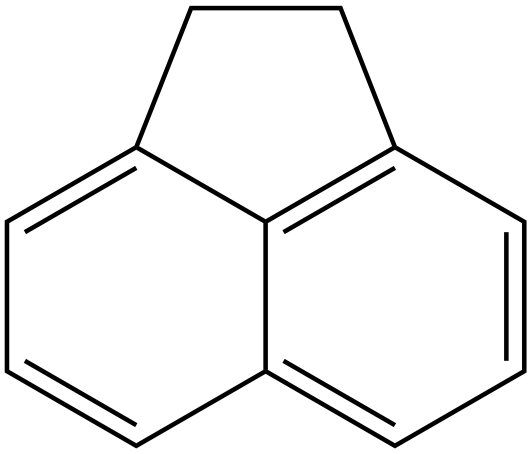

(e) Acenaphthene

Figure 4.2: Chemical structures of all four precursors and acenaphthene (impurity for acenaphthylene).

4.2 Data analysis

In this work, I will not go into the details of AMS data analysis, as this would also require a more detailed instrumentation description and thereby only the main analysis parts are mentioned here. However, the data analysis is a crucial part for correct identification of the fragments detected with the AMS.

Firstly, a m/z calibration is performed: the time-of-flight data from the raw spectra is converted to m/z values. This is done by choosing a few peaks with known m/z values and using them to calculate the m/z values for the rest of the data. There are few criteria for the peaks used in the m/z calibration. One must know exactly which ions are used so that the correct m/z value are set for the peak. The ions used for the m/z calibration should also cover a wide range of masses, so that peaks at both low and high masses are pinpointed correctly to the right m/z values.

After the m/z calibration a baseline is calculated. This takes into account the background signal that is measured with the chopper (open and closed mode), described previously in Section 3.1.2. Next is the peak shape and width determination. During this step, a function is fitted to the measured signal (see Appendix A for visualisation of this). This step is also crucial for high resolution data analysis: with wrong peak shape and width, small-signal ions close to bigger peaks can be lost during this step. When all of the peak shape parameters are determined, one must still manually go through all ions and choose which should be fitted. After this there are still a few steps before the final processed data is ready.

A more detailed description of high resolution AMS data analysis can be found in [DeCarlo et al., 2006].

All of the data analysis for AMS data is done with two AMS analysis packages implemented in the data analysis software Igor Pro by WaveMetrics Inc. The two AMS packages, developed by Aerodyne, is SQUIRREL (SeQUential Igor data RetRiEvaL) and PIKA (Peak Integration by Key Analysis). The software versions used in this work was Igor Pro 6.37, SQUIRREL 1.62A and PIKA 1.22A.

All of the data analysis for this work was done by me.

5. Results and discussion

In this chapter the time series of all experiments are presented, showing the mass concentration evolution during each experiment. Main emphasis is put on the mass spectral differences for the different precursors and the NO_x^+ ratio detected and comparing them to previous studies.

5.1 Time series

In this section the time series and mass concentrations for organics, nitrates and the nitrate to organic ratios (NO_3:Org) of all four precursor experiments are presented in Figure 5.1. The green line represents the organics, the blue one is nitrates and the orange line is the NO_3:Org ratio. The NO_3:Org ratio for all experiments are presented in Figure 5.2. During the measurements, the pON particle concentration was stepwise increased or decreased to cover a wider range of mass concentrations and can be seen as stable plateaus in the organic and nitrate mass concentrations. Particle concentrations for the different steps are shown in Table 5.1. All of the data were measured with 1 minute time resolution.

Table 5.1: Measurement steps: showing the selected particle size and number concentration for different steps for all pON precursor VOCs.

	Acenaphthylene	Guaiacol	Limonene	β-pinene
d_a (nm)	300	200	300	400
Step 1 (cm^{-3})	800	3200	480	400
Step 2 (cm^{-3})	1500	7300	750	250
Step 3 (cm^{-3})	2800	11000	1100	180
Step 4 (cm^{-3})	3500	18000	1600	-
Step 5 (cm^{-3})	-	26000	-	-

5.1.1 Acenaphthylene

The time series of acenaphthylene + NO_3 measurement from 11 Dec 2018 is presented in Figure 5.1a. Particle size was selected to 300 nm. The particle concentration was increased stepwise ranging from $8{\cdot}10^2$ to $3.5{\cdot}10^3$ cm^{-3}. The organic and nitrate mass concentrations was measured to range from 1.7 to 9.9 and 1.0 to 5.4 µg m^{-3}, respectively. The NO_3:Org ratio was stable during the whole experiment: 0.55 ± 0.010 (one standard deviation).

5.1.2 Guaiacol

The time series of guaiacol + NO_3 measurements from 7 Dec 2018 is presented in Figure 5.1c. Particle size was selected to 200 nm. The particle concentration was increased stepwise ranging from $3.2{\cdot}10^3$ to $2.6{\cdot}10^5$ cm^{-3}. The organic and nitrate mass concentrations was measured to range from 4.1 to 47 and 0.59 to 5.9 µg m^{-3}, respectively. The NO_3:Org ratio was 0.14 ± 0.050 (one standard deviation)

5.1.3 Limonene

The time series of limonene + NO_3 measurements from 3 Dec 2018 is presented in Figure 5.1d. Particle size was selected to 300 nm. The particle concentration was increased stepwise ranging from $4.8{\cdot}10^2$ to $1.6{\cdot}10^3$ cm^{-3}. The organic and nitrate mass concentrations was measured to range from 3.1 to 16 and 0.69 to 3.3 µg m^{-3}, respectively. The NO_3:Org ratio was 0.21 ± 0.007 (one standard deviation).

5.1.4 β-pinene

The time series of β-pinene + NO_3 measurements from 6 Dec 2018 is presented in Figure 5.1b. Particle size was selected to 400 nm. The particle concentration was decreased stepwise ranging from $4.0{\cdot}10^2$ to $1.8{\cdot}10^2$ cm^{-3}. The organic and nitrate mass concentrations was measured to range from 12 to 3.8 and 1.7 to 0.54 µg m^{-3}, respectively. The NO_3:Org ratio was 0.14 ± 0.002 (one standard deviation).

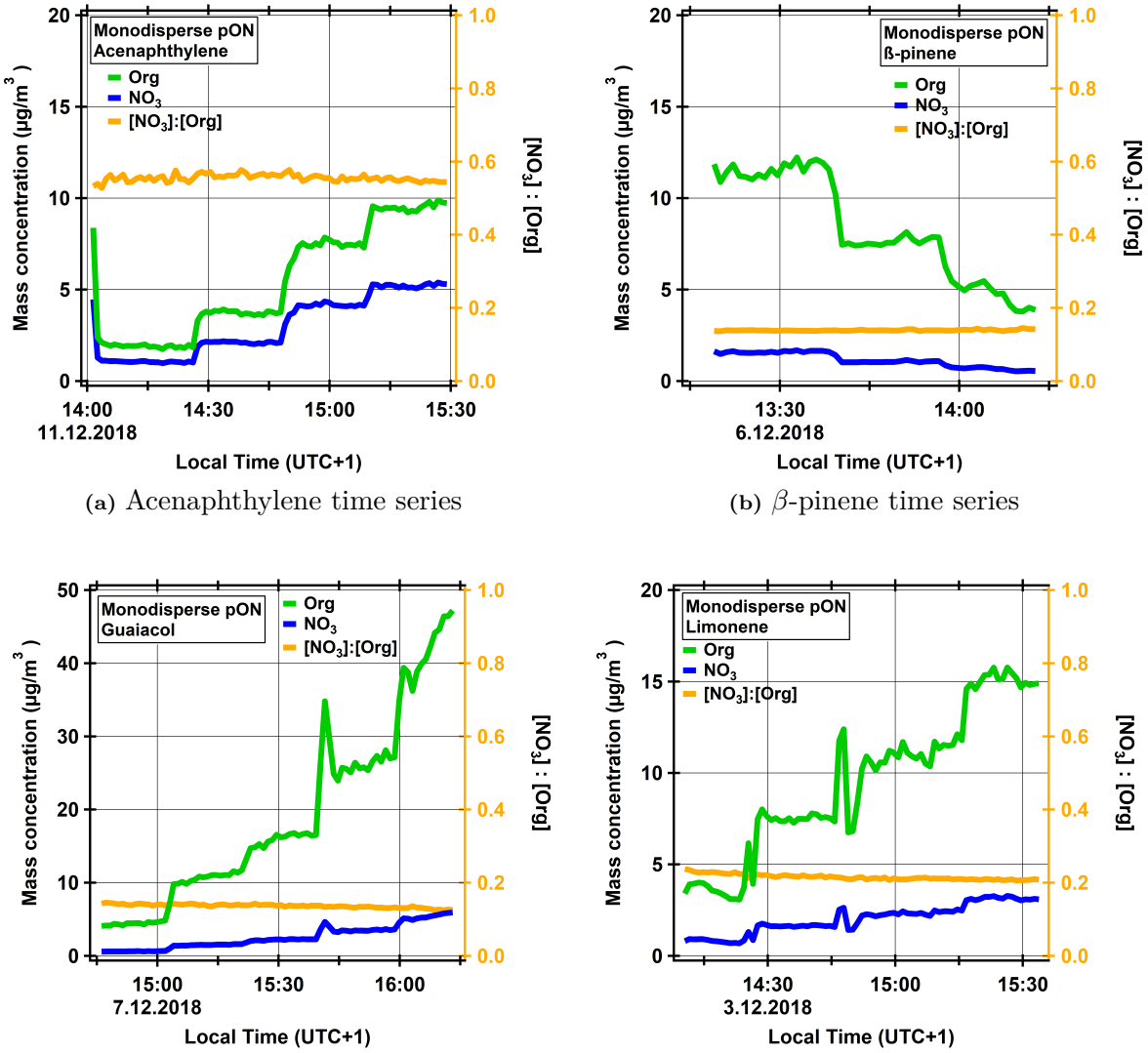

(a) Acenaphthylene time series

(b) β-pinene time series

(c) Guaiacol time series

(d) Limonene time series

Figure 5.1: Time series of all four precursor experiments, showing the mass concentration of organics and nitrates and the organic to nitrate ratio. a) is for acenaphthylene, b) for β-pinene, c) for guaiacol and d) for limonene.

5.2 Mass spectral differences

The individual mass spectrum of all four precursor experiments are presented in Figures 5.3 to 5.6 and in Figure 5.7 all four mass spectrum are in the same figure to ease the comparision. The fraction of every organic family, CH, CHO1, CHOgt1, CHN, CHO1N, CHOgt1N (were gt1 stand for *greater than 1*, meaning that in those fragments there are more than one oxygen atom), is shown in Figure 5.8. In the organic families, the number of carbon, hydrogen and nitrogen atoms are not specified whereas the number of oxygen atoms is specified as one or more than one. The nitrate to organic ratio for all four experiments are shown in Figure 5.2. All of the

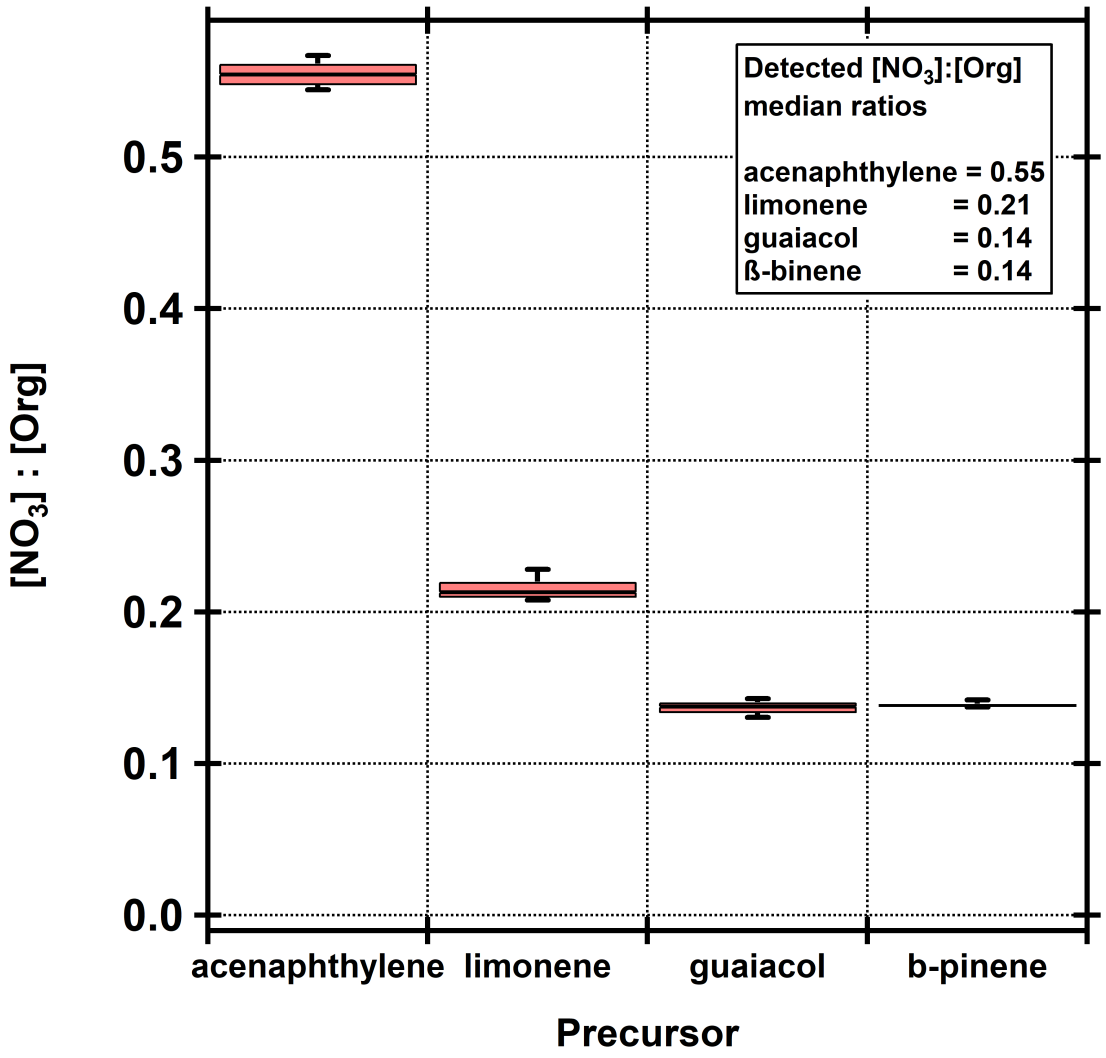

Figure 5.2: Median nitrate to organic ratio.The boxes represent the 25$^{\text{th}}$ and 75$^{\text{th}}$ percentile, whiskers are the 10$^{\text{th}}$ and 90$^{\text{th}}$ percentile.

nitrogen-containing organic fragments ($C_xH_yO_zN_p$ fragments, where $x, y, z, p > 0$) detected are listed in Tables 5.2 to 5.4, where the fragments coloured in red are unique fragments that are detected only for one precursor and could possibly be used as tracers. In Appendix A, there are a few screenshots from the data analysis part to see how well the L-ToF-AMS is able to separate fragments with small mass-difference. From there it is also seen that most of the $C_xH_yO_zN_p$ fragments are very small (often only a few percent of the total signal at its unit mass) and close to other fragments, and even higher resolution is needed to separate these.

The acenaphthylene + NO_3 mass spectrum (Figure 5.3) is dominated by simple hydrocarbon (CH) fragments, although the NO^+ fragment is the largest single peak with its over 20% relative contribution to the total detected signal. The CH fragments

accounts for nearly 70% of the total organic signal, while the contribution the nitrogen containing families, CHN, CHNO1 and CHOgt1N, the contributions are small: 0.3%, 0.7% and 0.7%, respectively. Unlike the other investigated precursors, acenaphthylene has many of its organic fragments at high m/z values: several CH and some CHO1 fragments are at $m/z > 110$. Nitrogen-containing organic fragments that are a major peak at its unit mass are found at $m/z = 57$, 58, 69 and 70. Acenaphthylene has the highest nitrate to organic ratio, 0.55, indicating that a large fraction of its pON is fragmented to NO^+ and NO_2^+.

In the β-pinene + NO_3 organic mass spectrum (Figure 5.4), CH and CHO1 fragments (69% and 28%) accounts for over 96% of all signal, leaving the contribution of CHOgt1, CHN, CHO1N and CHOgt1 fragments to 2.6%, 0.3%, 0.08% and 0.3%. Similar to acenaphthylene, NO^+ is the largest single fragment. However, its relative contribution is only 8% of the total signal. Together with guaiacol, β-pinene has the lowest nitrate to organic ratio, 0.14 and no major $C_xH_yO_zN_p$ fragments were detected.

The limonene + NO_3 organic mass spectrum (Figure 5.5) is dominated by CH and CHO1 fragments, they contribute 50% and 46% of all organic signal. The high CHO1 fraction is due to the large peak at m/z 43 and the $C_2H_3O^+$ fragment, it is the largest single fragment detected and stands alone for almost 20% of the total signal in the mass spectra. CHOgt1 accounts for 3% and all the nitrogen-containing families contribute 0.8% each. Limonene produced least $C_xH_yO_zN_p$ fragments, only 14 fragments were detected. In addition to this, all of its $C_xH_yO_zN_p$ fragments were detected at such unit masses where $C_xH_yO_zN_p$ fragments for the other precursors were also detected, so limonene as pON precursor can not be identified by these fragments. The nitrate to organic ratio was 0.21.

The guaiacol + NO_3 organic mass spectrum (Figure 5.6) is the only where the CH is not the largest organic family, here the largest family is CHO1 with its 38% contribution, while CH stands for 27% and CHOgt1 26% of the organics. The high CHO1 fraction is mainly due to the fragments at m/z 28 (CO^+) and 29 (CHO^+), each accounts for 7 to 8% of the total signal in the guaiacol mass spectra. Guaiacol has by far the highest amount of nitrogen containing fragments: CHN, CHO1N and CHOgt1N accounts for 4%, 1% and 0.6% of the organics. From this experiment, the largest amount (over 40) of nitrogen-containing organic fragments were detected, but only at $m/z = 67$, 68 and 80 it was the major fragment at that unit mass. The rest of the $C_xH_yO_zN_p$ fragments did not contribute significantly to the signal at its unit mass. The nitrate to organic ratio was 0.14. The CHOgt1N fragments in the organic mass

spectra (Figure 5.6) looks unusual, especially as it contains several fragments at $m/z >$ 130. Although there are many of these fragments, their contribution to the total organic mass spectrum is, as earlier mentioned, only 0.6%, meaning that these fragments are small. One explanation to the vast amount of these CHOgt1N fragments might be related to errors in the peak shape determination or the m/z calibration during the data analysis. This is possible because during the HR-analysis one is required to choose every fragment that are being fitted to the collected raw data. If the raw data signal is noisy or several fragments are close each other, such errors may happen. This opens up the possibility for errors and leads to choosing fragments that actually are not there because the raw data is not properly processed. Further work will explore the validity of these results in more detail.

5.3 NO_x^+ ratios

In this section, the detected NO^+ to NO_2^+ ratio (NO_x^+ ratio) for all four precursors are presented in Figure 5.9. For all four precursors, a straight line was fitted to the NO^+ and NO_2^+ data to get the NO_x^+ ratio as the slope of the fit. The linear fit is very good (Pearson correlation coefficient, r, is over 0.99 for all four cases) for all four precursors, as shown in Figure 5.11.

The median NO_x^+ ratio was quite similar for all four precursors, the highest NO_x^+ ratio was measured for acenaphthylene (6.70), followed by guaiacol (6.60), β-pinene (6.23) and limonene (5.96). When comparing our measured NO_x^+ ratios with previous studies with same precursors and NO_3 oxidation (see Figure 5.10), large variation is seen especially for β-pinene. All other studies were carried out with a HR-ToF-AMS, also taking into account the CH_2O^+ fragment at m/z 30 when calculating the NO^+ signal. One reason to the variation might be instrumental bias, discussed already in [Boyd et al., 2015], and as no previous study has been done with the L-ToF-AMS, a new instrumental bias might occur. For acenaphthylene there were no previous studies, but the purity of only 75% (rest acenaphthene) must be remembered when future studies are compared to these results.

Table 5.2: Detected $C_xH_yO_zN_p$ fragments between m/z 43 and 89. Fragments coloured in red are unique fragments that are detected only for one precursor. All of the fragments are positive ions.

m/z	Acenaphthylene	Guaiacol	Limonene	β-pinene
43	CHNO	CHNO		
44				
45			CH_3NO	CH_3NO
46				
47			CH_5NO	CH_5NO
48				
54		C_2HNO		
55	C_2HNO			
56	C_2H_2NO	C_2H_2NO		
57	$C_4H_6NO_2$	C_2H_3NO		C_2H_3NO
58	C_2H_4NO	C_2H_4NO		C_2H_4NO
59				C_2H_5NO
60		CH_2NO_2	C_2H_6NO	C_2H_6NO
			CH_2NO_2	CH_2NO_2
61		CH_3NO_2		
62				CH_4NO_2
63				CH_5NO_2
64				
67	C_3HNO	C_3HNO		
68	C_3H_2NO	C_3H_2NO		
69	C_3H_3NO			
70	C_3H_4NO	C_3H_4NO		
71				C_3H_5NO
72		$C_2H_2NO_2$		C_3H_6NO
73				$C_2H_5N_2O$
74				
75				$C_2H_5NO_2$
76			CH_2NO_3	CH_2NO_3
77				
78		C_4NO		
79				
80		C_4H_2NO		
81				
82				
86		$C_3H_4NO_2$		$C_3H_4NO_2$
87	C_4H_9NO	$C_3H_5NO_2$		
88			$C_3H_6NO_2$	$C_3H_6NO_2$
89				

Table 5.3: Detected $C_xH_yO_zN_p$ fragments between m/z 90 and 139. Fragments coloured in red are unique fragments that are detected only for one precursor. All of the fragments are positive ions.

m/z	Acenaphthylene	Guaiacol	Limonene	β-pinene
90		$C_2H_4NO_3$		
91				
92				
98		$C_4H_4NO_2$		
100	$C_5H_{10}NO$			
101			$C_4H_7NO_2$	$C_4H_7NO_2$
102		$C_3H_4NO_3$		
103				
104		$C_3H_6NO_3$		
105				
106				
109		C_6H_7NO		
110				
111				
112		$C_5H_6NO_2$		
113				
114				
117	$C_5H_{11}NO_2$			
118				
120	$C_6H_2NO_2$			
121	$C_5HN_2O_2$			
122				
128		$C_4H_2NO_4$		$C_6H_{10}NO_2$
129				
132		$C_4H_6NO_4$		$C_4H_6NO_4$
133	$C_4H_7NO_4$	$C_3HN_2O_5$		
134	$C_7H_6N_2O$			
135				
136		$C_6H_2NO_3$		
137				
138		$C_6H_4NO_3$		
139		$C_6H_5NO_3$		

Table 5.4: Detected $C_xH_yO_zN_p$ fragments between m/z 140 and 160. Fragments coloured in red are unique fragments that are detected only for one precursor. All of the fragments are positive ions.

m/z	Acenaphthylene	Guaiacol	Limonene	β-pinene
140		$C_5H_2NO_4$		
		$C_6H_6NO_3$		
141	$C_5H_5N_2O_3$	$C_5H_5N_2O_3$	$C_7H_{11}NO_2$	
	$C_6H_7NO_3$	$C_6H_7NO_3$		
		$C_7H_{11}NO_2$		
		$C_5H_3NO_4$		
142	$C_6H_8NO_3$	$C_6H_8NO_3$	$C_6H_8NO_3$	$C_6H_8NO_3$
		$C_5H_4NO_4$	$C_7H_{12}NO_2$	
143		$C_5H_5NO_4$	$C_6H_9NO_3$	
			$C_7H_{13}NO_2$	
144		$C_5H_6NO_4$		$C_5H_6NO_4$
				$C_7H_{14}NO_2$
145	$C_6H_{11}NO_3$	$C_5H_7NO_4$		$C_7H_{15}NO_2$
		$C_6H_{11}NO_3$		
146				
147	$C_5H_9NO_4$			
148	$C_7H_2NO_3$	$C_7H_2NO_3$		$C_5H_{10}NO_4$
	$C_5H_{10}NO_4$	$C_5H_{10}NO_4$		
149				
150				
151		$C_7H_5NO_3$		
152		$C_6H_2NO_4$		
		$C_7H_6NO_3$		
153		$C_6H_3NO_4$	$C_9H_{15}NO$	$C_9H_{15}NO$
		$C_7H_7NO_3$		
154	$C_7H_8NO_3$	$C_7H_8NO_3$		
		$C_6H_4NO_4$		
155	$C_7H_9NO_3$	$C_7H_9NO_3$		$C_7H_9NO_3$
		$C_6H_5NO_4$		
156	$C_7H_{10}NO_3$	$C_7H_{10}NO_3$	$C_7H_{10}NO_3$	
		$C_6H_6NO_4$		
157		$C_6H_7NO_4$	$C_7H_{11}NO_3$	$C_7H_{11}NO_3$
158		$C_6H_8NO_4$	$C_6H_8NO_4$	$C_6H_8NO_4$
159		$C_6H_9NO_4$		$C_6H_9NO_4$

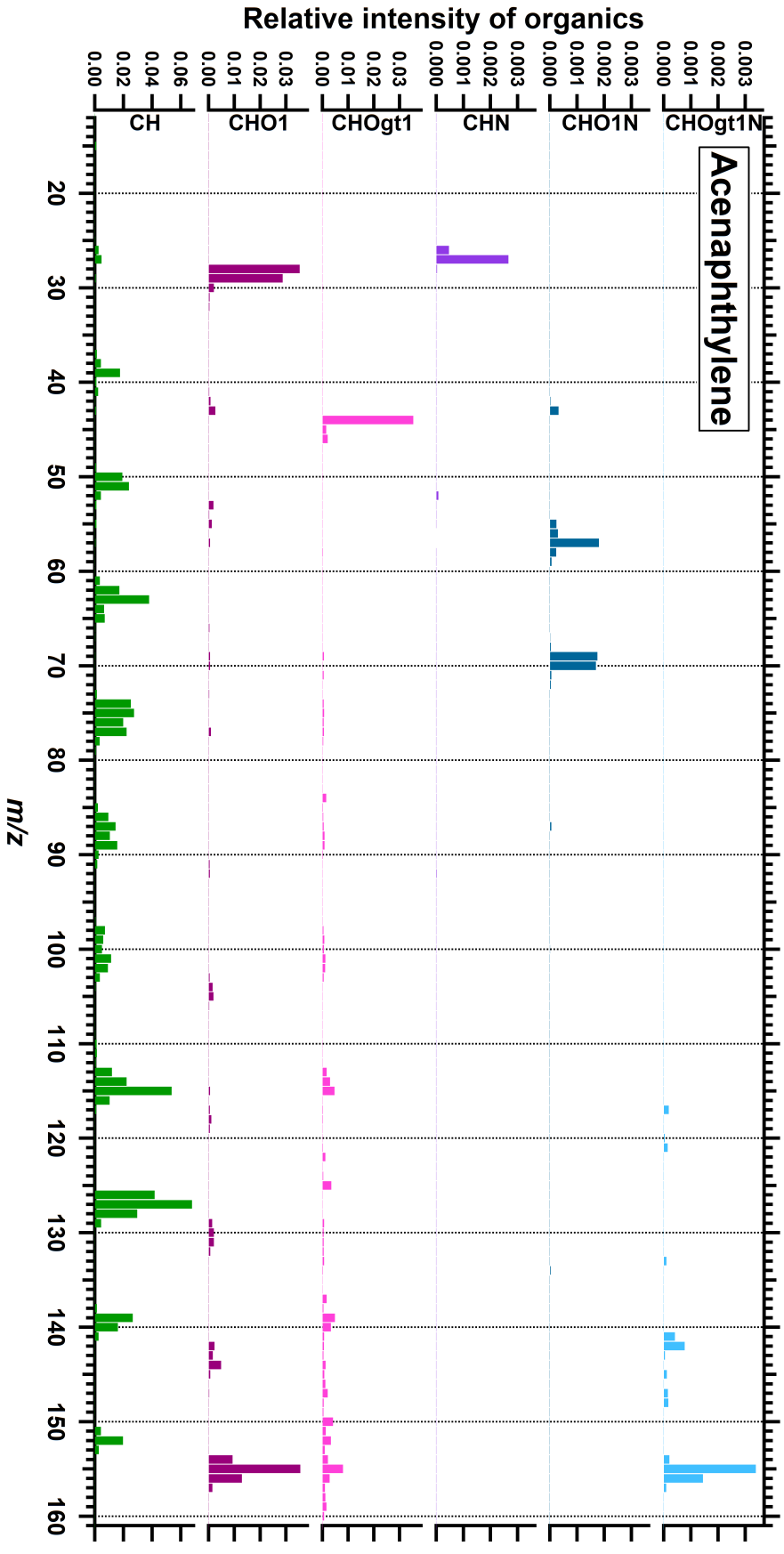

Figure 5.3: Mass spectrum of organic fragments from the acenaphthylene + NO_3 experiment. Mass spectrum separated by organic family.

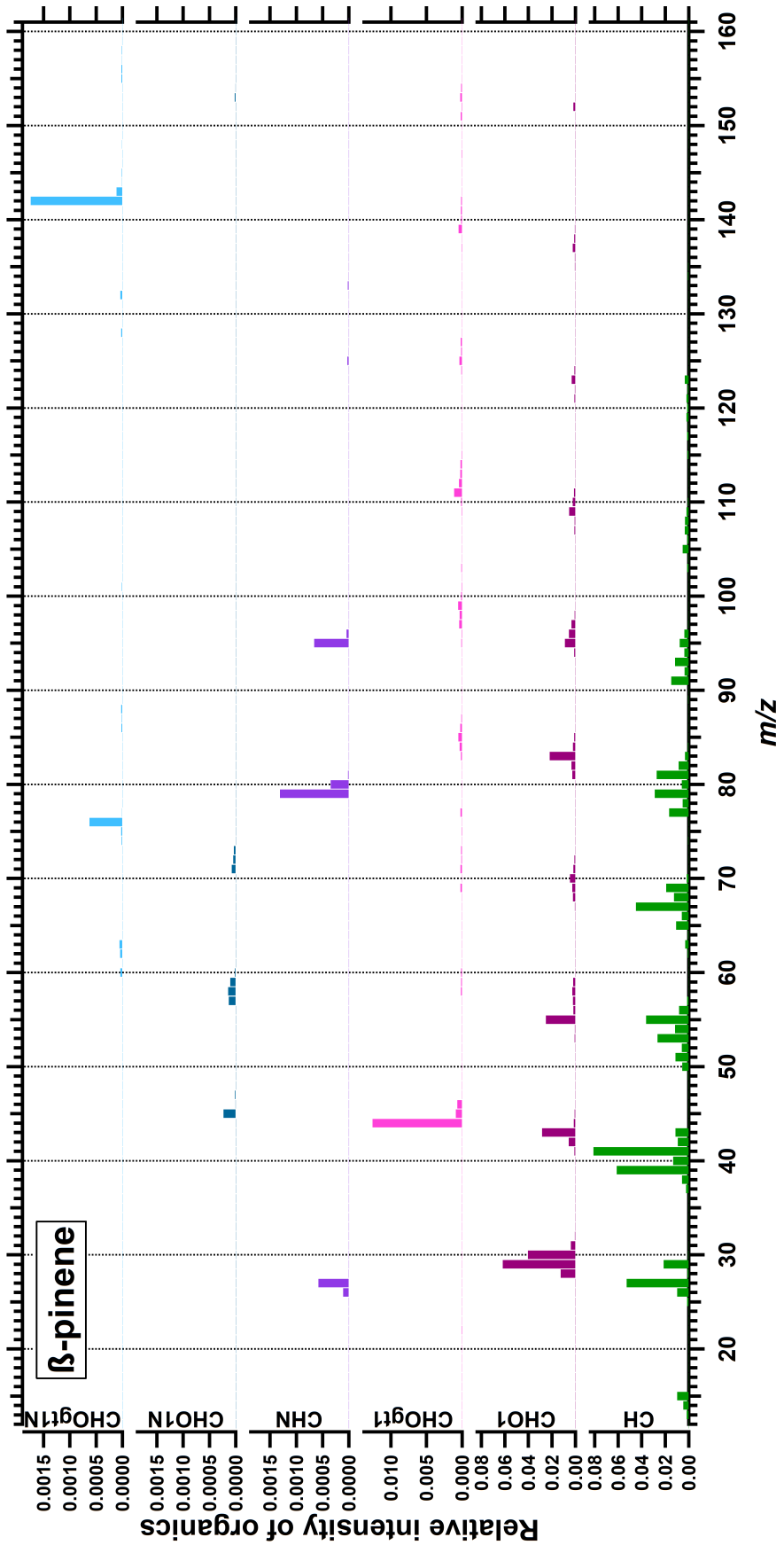

Figure 5.4: Mass spectrum of organic fragments from the β-pinene + NO_3 experiment. Mass spectrum separated by organic family.

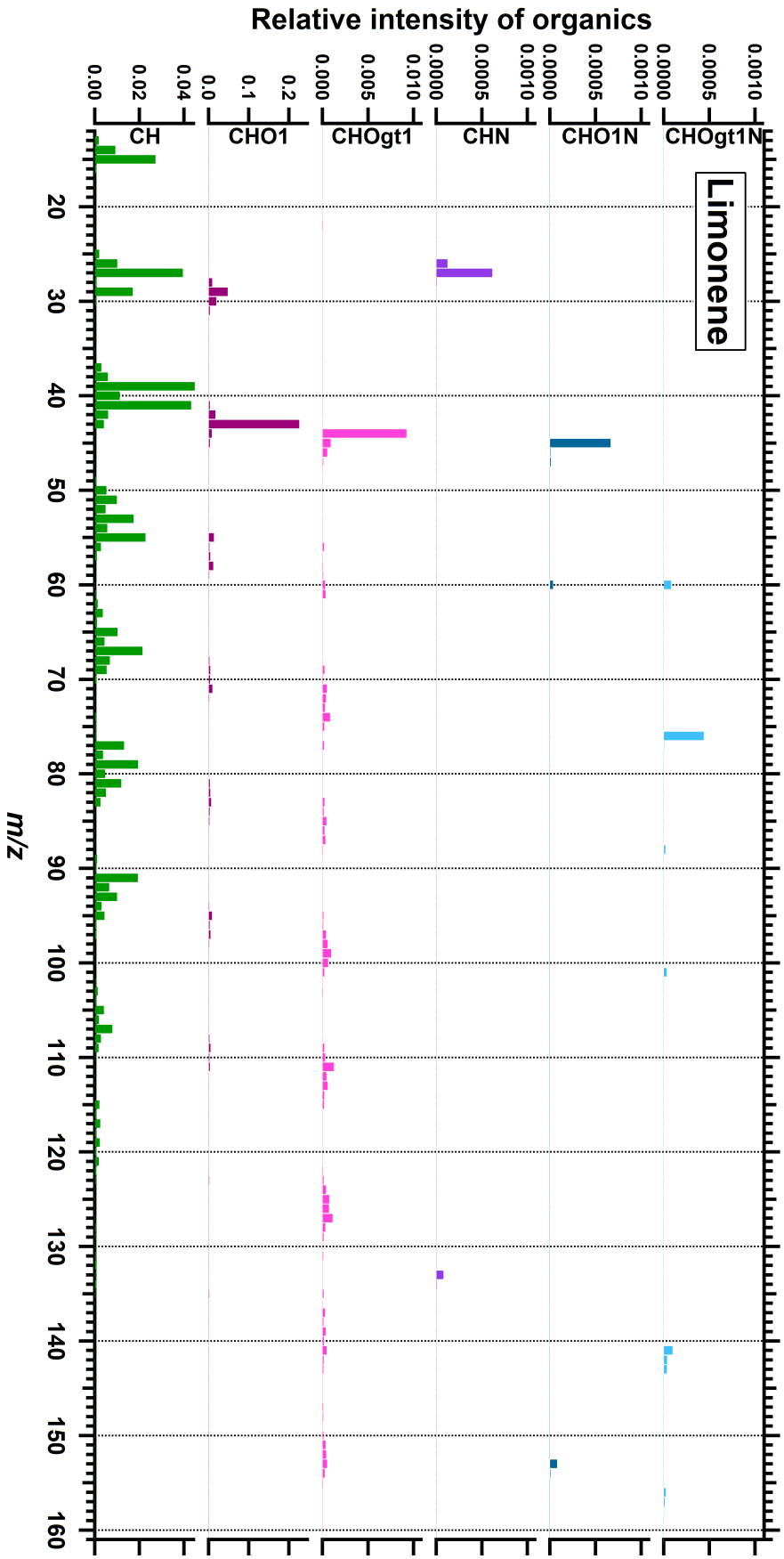

Figure 5.5: Mass spectrum of organic fragments from the limonene + NO_3 experiment. Mass spectrum separated by organic family.

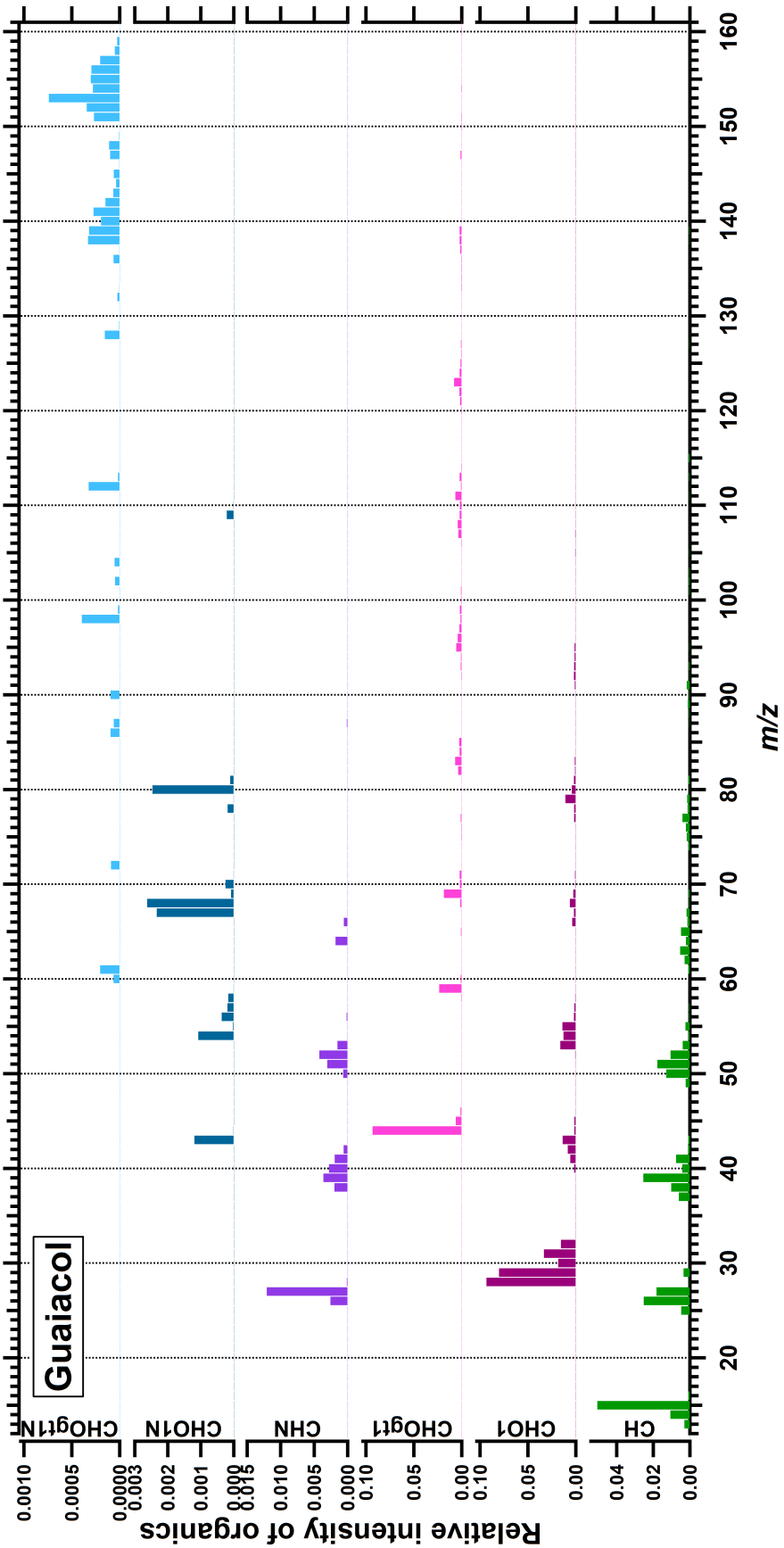

Figure 5.6: Mass spectrum of organic fragments from the guaiacol + NO_3 experiment. Mass spectrum separated by organic family.

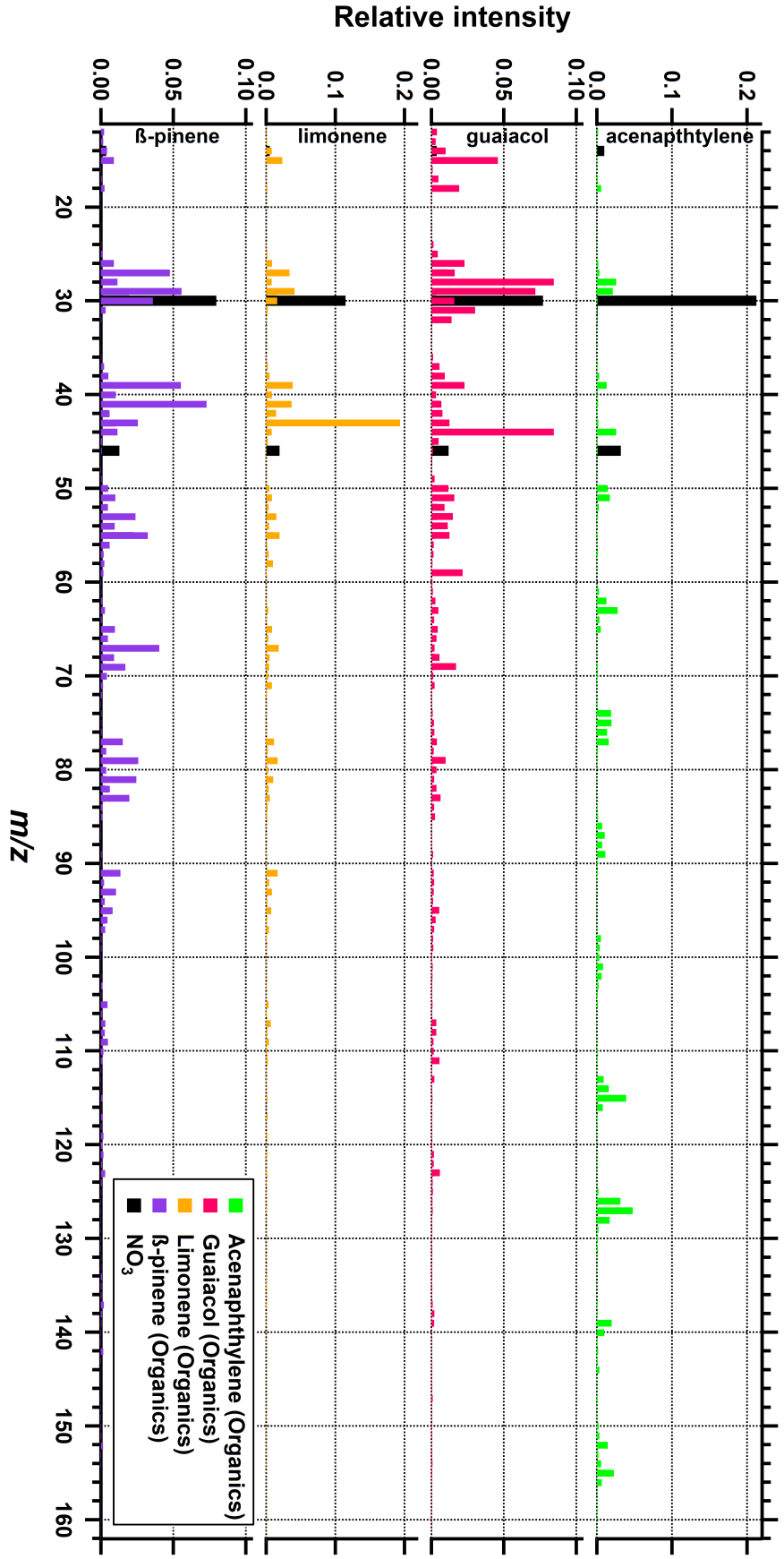

Figure 5.7: Mass spectrum of all four precursor experiments.

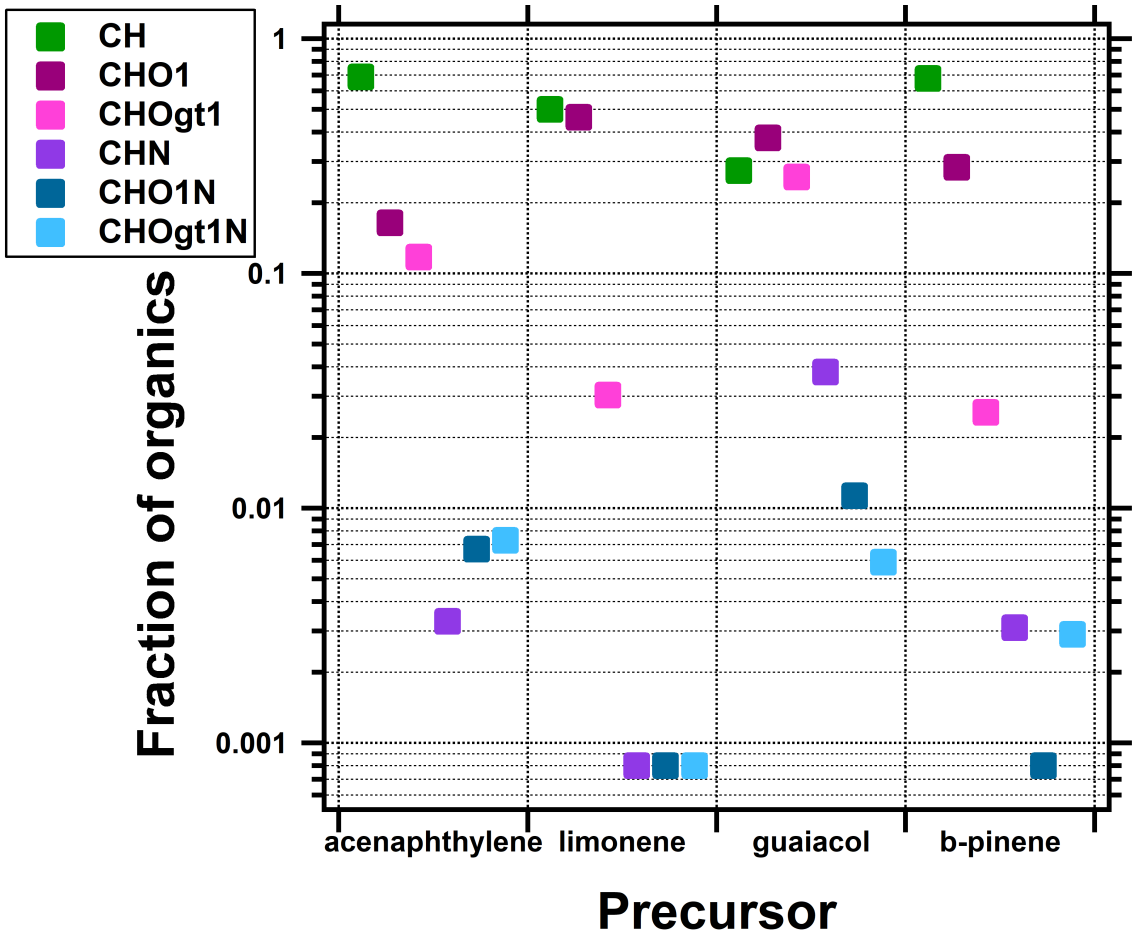

Figure 5.8: The organic families fraction of the total organic signal for each precursor.

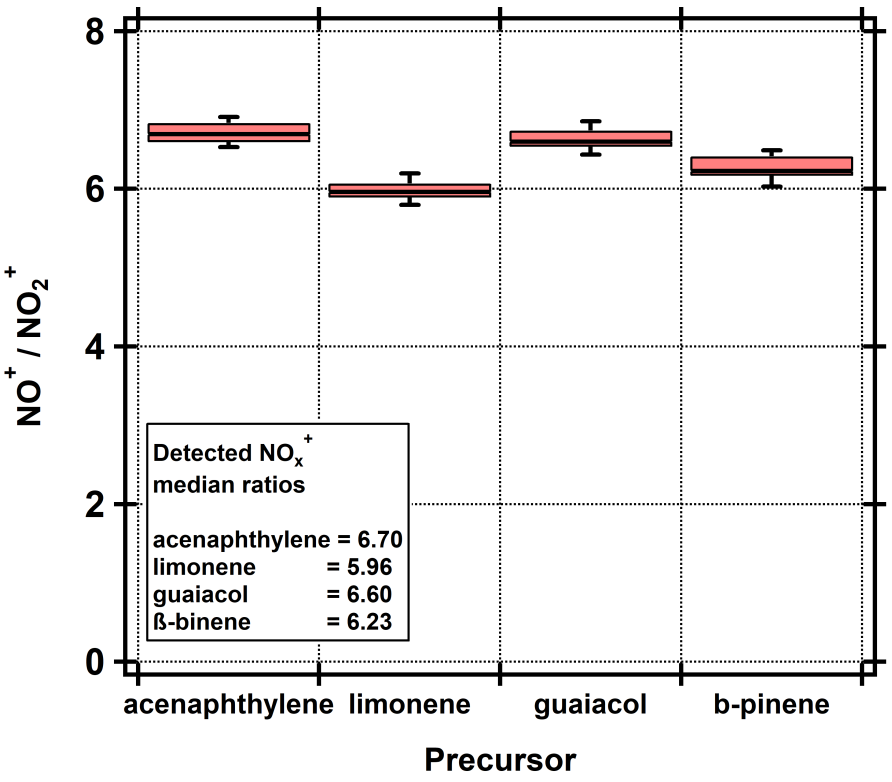

Figure 5.9: Detected median values for the NO_x^+ ratio for all 4 precursors. The boxes represent the 25th and 75th percentile, whiskers are the 10th and 90th percentile.

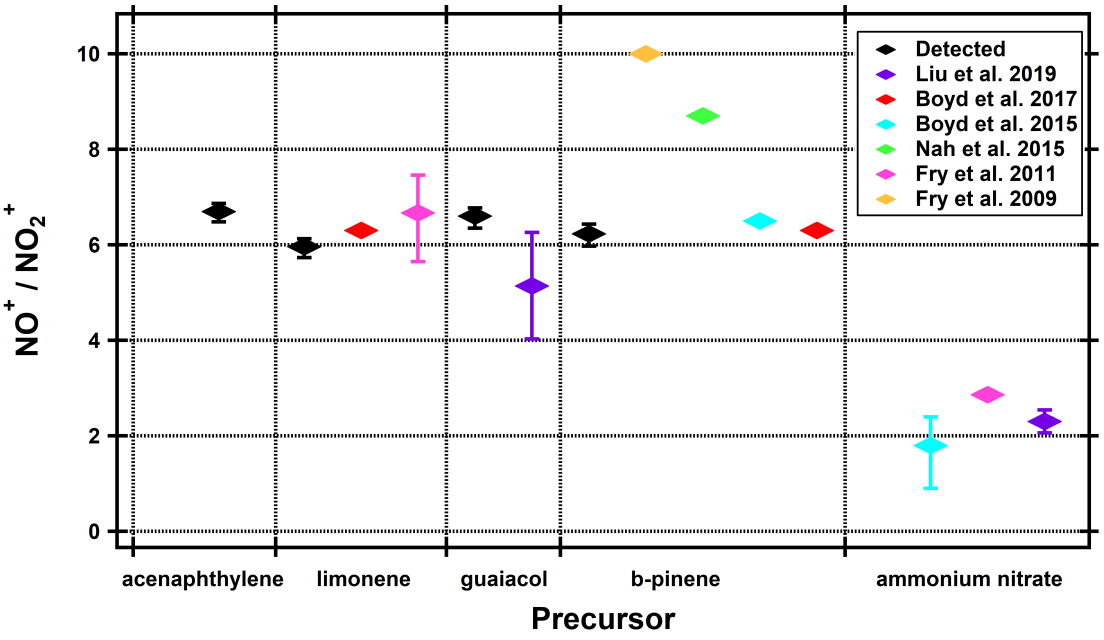

Figure 5.10: Detected and literature values for NO_x^+ ratios for all 4 precursors and ammonium nitrate. Black markers are values measured during this work, rest is previous studies.

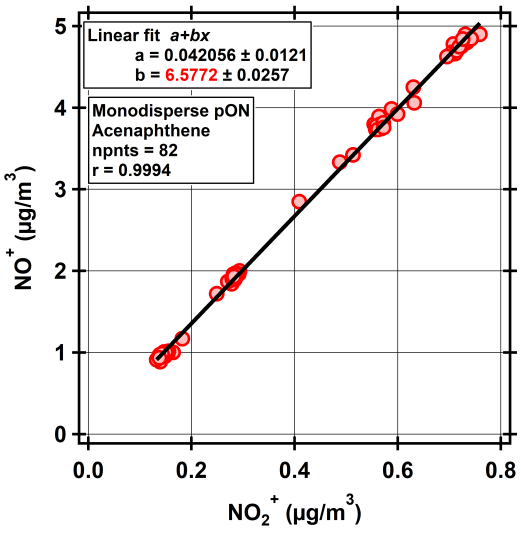

(a) Acenaphthylene

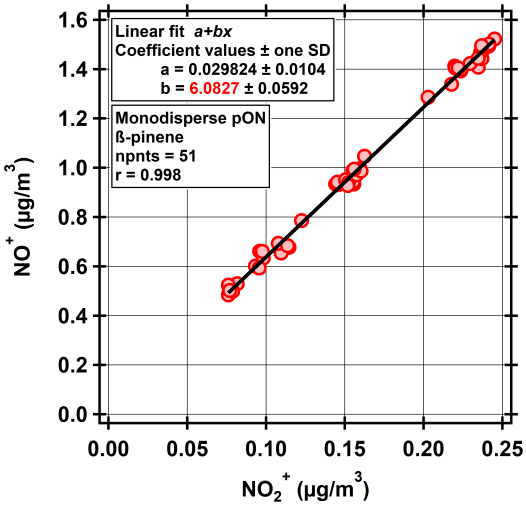

(b) β-pinene

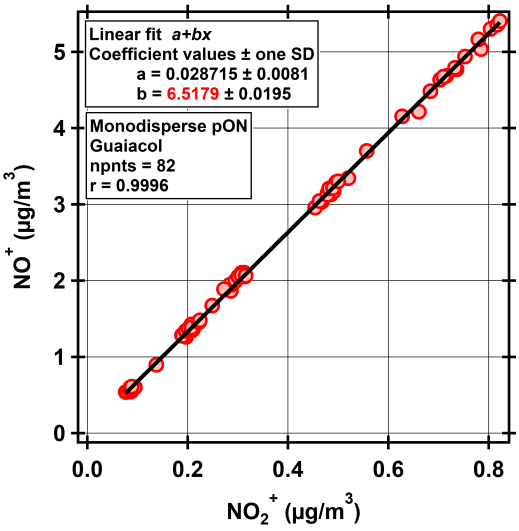

(c) Guaiacol

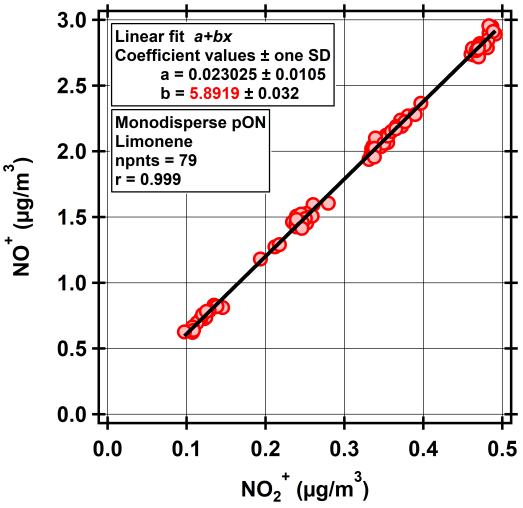

(d) Limonene

Figure 5.11: NO_x^+ ratio for all four precursors.

6. Conclusions

At the ACMCC, we generated monodisperse pON in a PAM-chamber by oxidizing four different VOCs with NO_3 radicals and sampled it with 8 ACSM instruments as well as a L-ToF-AMS that I operated. I investigated the fragments produced in the AMS by utilizing the high resolution of the L-ToF-AMS, and was able to separate fragments with different elemental composition and divide them into different organic families. VOCs used in the work was β-pinene, limonene, guaiacol and acenaphthylene.

Using the NO_x^+ ratio for separating and quantifying organic nitrate from inorganic nitrate has been previously suggested, and in this work we measured quite similar NO_x^+ ratio for all four pON-precursors. Our measured NO_x^+ ratios are in good consistent with most previous studies, although some studies differ from our results. The measured NO_x^+ ratio in our experiments for all four precursors are within the range of 6.3 ± 0.4.

The main focus in this work was investigating the differences in the fragmentation patterns for the different precursors and detecting $C_xH_yO_zN_p$-fragments, something that has been previously challenging due to limitations of the AMSs resolution. During this work, I tentatively detected over 100 different $C_xH_yO_zN_p$-fragments, which can now possibly be used as marker fragments for these precursors in ambient measurements. Especially for the guaiacol and acenaphthylene experiments, I found several unique $C_xH_yO_zN_p$-fragments. Although the L-ToF-AMS has higher resolution than any older AMS version and is capable of separating $C_xH_yO_zN_p$-fragments, there are still some uncertainties, mainly linked to possible problems with the m/z calibration and the peak shape determination during the data analysis. Because the $C_xH_yO_zN_p$-fragments are often very small and close to some other fragment, they might appear in the data analysis even though they would not actually be present. Actual fragments might also be lost with this kind of problems. This is an aspect that always must be considered when analysing L-ToF-AMS data.

As shown in this and previous studies, the oxidation of BVOCs with NO_3 radicals are a direct link between natural and anthropogenic emissions and aerosol formation. These results can also be utilized in the improvement of the fragmentation table for UMR instruments (for example the ACSM) and source apportionment of SOA formation.

Future research should focus on quantifying the aerosol yield from BVOC + NO_3 reactions and studying the particle phase evolution of pON. In this work, we used only particle phase instruments, but combining these results with gas-phase measurements could give us crucial new information about pON and NO_x cycling in the atmosphere and reduce the gap between measurements and theory. This knowledge is essential for the quantification of pON yields.

A. Peak fitting during L-ToF-AMS data analysis

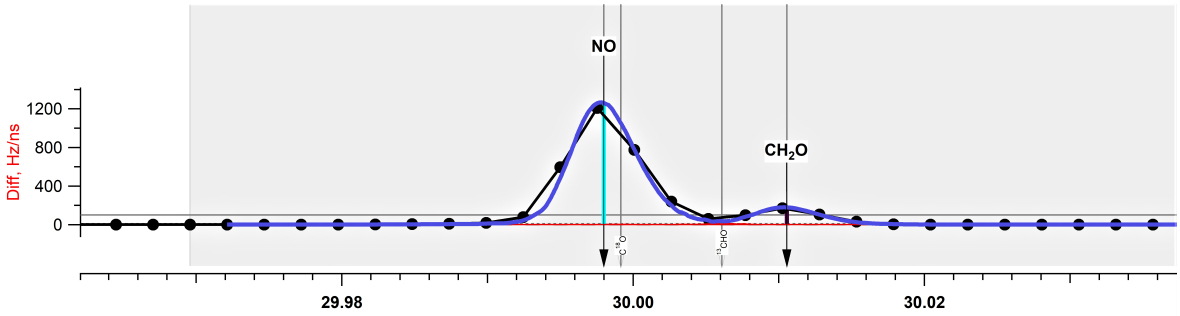

Figure A.1: Screenshot from peak-fitting during the data-analysis when choosing which fragments contributes to each signal. At $m/z = 30$ from the limonene + NO_3 experiment, we have the NO^+ and CH_2O^+ fragments. The black dotted line represents the raw data from the AMS and the blue one is the fitted sum-line for all fragments.

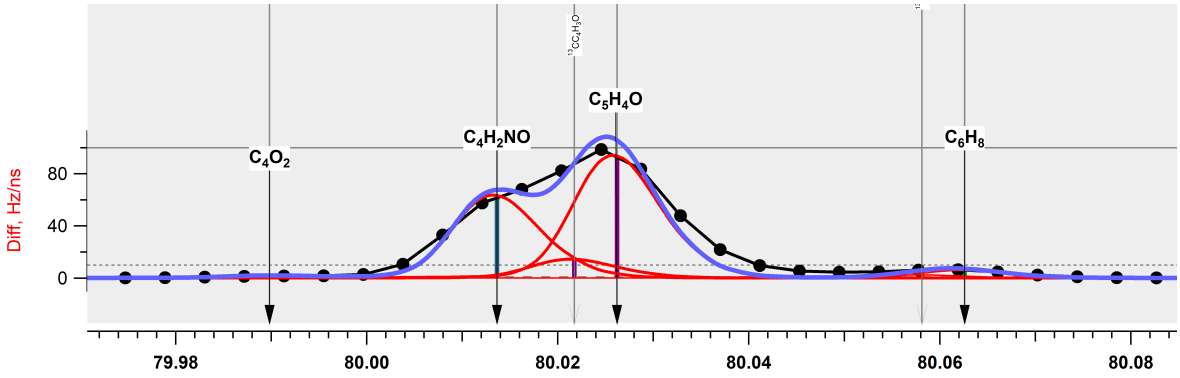

Figure A.2: Screenshot from peak fitting during the data analysis when choosing which fragments contributes to each signal. At $m/z = 80$ from the guaiacol + NO_3 experiment, we have $C_4H_2NO^+$ and $C_5H_4O^+$ as the main fragments. The black dotted line represents the raw data from the AMS, the red ones are fitted peaks for each fragment and the blue line is the fitted sum-line for all fragments. We can see here that the fitted blue line do not perfectly line up with the black raw data.

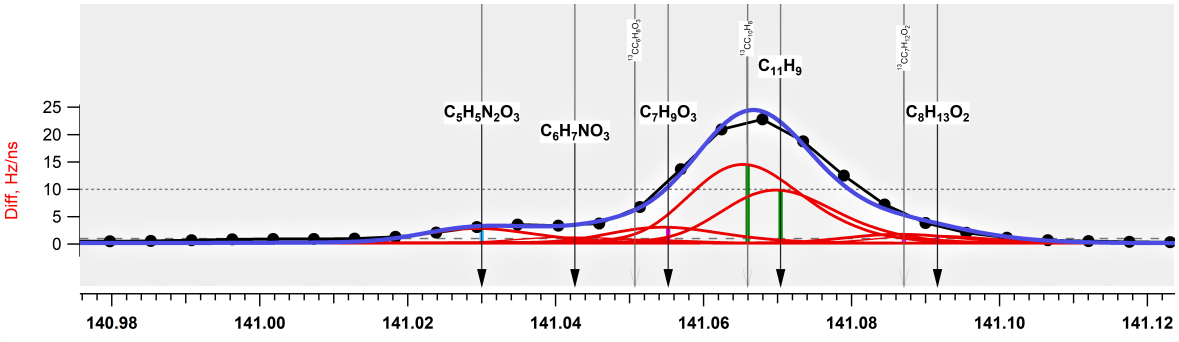

Figure A.3: Screenshot from peak fitting during the data analysis when choosing which fragments contributes to each signal. At $m/z = 141$ from the acenapthtylene + NO_3 experiment, we have several fragments that can not be separated. The black dotted line represents the raw data from the AMS, the red ones are fitted peaks for each fragment and the blue line is the fitted sum-line for all fragments. Here we can see that the individual fragments can not be separated, but summed up together they represent the detected raw data.

Bibliography

[Abbey et al., 1999] Abbey, D. E., Nishino, N., McDonnell, W. F., Burchette, R. J., Knutsen, S. F., Lawrence Beeson, W., and Yang, J. X. (1999). Long-term inhalable particles and other air pollutants related to mortality in nonsmokers. *American journal of respiratory and critical care medicine*, 159(2):373–382.

[Aerodyne,] Aerodyne. *Aerodyne Webpage*. http://www.aerodyne.com/products/aerosol-mass-spectrometer(accessed October 12, 2019).

[Alfarra, 2004] Alfarra, M. (2004). *Insights into atmospheric organic aerosols using an aerosol mass spectrometer*. PhD thesis, University of Manchester Manchester, UK.

[Allan et al., 2004] Allan, J. D., Bower, K. N., Coe, H., Boudries, H., Jayne, J. T., Canagaratna, M. R., Millet, D. B., Goldstein, A. H., Quinn, P. K., Weber, R. J., et al. (2004). Submicron aerosol composition at trinidad head, california, during itct 2k2: Its relationship with gas phase volatile organic carbon and assessment of instrument performance. *Journal of Geophysical Research: Atmospheres*, 109(D23).

[Atkinson and Arey, 2003] Atkinson, R. and Arey, J. (2003). Atmospheric degradation of volatile organic compounds. *Chemical reviews*, 103(12):4605–4638.

[Bouwman et al., 1997] Bouwman, A., Lee, D., Asman, W., Dentener, F., Van Der Hoek, K., and Olivier, J. (1997). A global high-resolution emission inventory for ammonia. *Global biogeochemical cycles*, 11(4):561–587.

[Boyd et al., 2015] Boyd, C., Sanchez, J., Xu, L., Eugene, A. J., Nah, T., Tuet, W., Guzman, M. I., and Ng, N. (2015). Secondary organic aerosol formation from the β-pinene+ no 3 system: effect of humidity and peroxy radical fate. *Atmospheric Chemistry and Physics*, 15(13):7497–7522.

[Boyd et al., 2017] Boyd, C. M., Nah, T., Xu, L., Berkemeier, T., and Ng, N. L. (2017). Secondary organic aerosol (soa) from nitrate radical oxidation of monoterpenes: effects of temperature, dilution, and humidity on aerosol formation, mixing, and evaporation. *Environmental science & technology*, 51(14):7831–7841.

[Brook, 2008] Brook, R. D. (2008). Cardiovascular effects of air pollution. *Clinical science*, 115(6):175–187.

[Canagaratna et al., 2007] Canagaratna, M., Jayne, J., Jimenez, J., Allan, J., Alfarra, M., Zhang, Q., Onasch, T., Drewnick, F., Coe, H., Middlebrook, A., et al. (2007). Chemical and microphysical characterization of ambient aerosols with the aerodyne aerosol mass spectrometer. *Mass spectrometry reviews*, 26(2):185–222.

[Chaloulakou et al., 2008] Chaloulakou, A., Mavroidis, I., and Gavriil, I. (2008). Compliance with the annual no2 air quality standard in athens. required nox levels and expected health implications. *Atmospheric Environment*, 42(3):454–465.

[Charlson, 1969] Charlson, R. J. (1969). Atmospheric visibility related to aerosol mass concentration. *Environmental science & technology*, 3(10):913–918.

[DeCarlo et al., 2006] DeCarlo, P. F., Kimmel, J. R., Trimborn, A., Northway, M. J., Jayne, J. T., Aiken, A. C., Gonin, M., Fuhrer, K., Horvath, T., Docherty, K. S., et al. (2006). Field-deployable, high-resolution, time-of-flight aerosol mass spectrometer. *Analytical chemistry*, 78(24):8281–8289.

[Dignon, 1992] Dignon, J. (1992). Nox and sox emissions from fossil fuels: A global distribution. *Atmospheric Environment. Part A. General Topics*, 26(6):1157–1163.

[Donahue et al., 2012] Donahue, N. M., Kroll, J., Pandis, S. N., and Robinson, A. L. (2012). A two-dimensional volatility basis set–part 2: Diagnostics of organic-aerosol evolution. *Atmospheric Chemistry and Physics*, 12(2):615–634.

[Farmer et al., 2010] Farmer, D., Matsunaga, A., Docherty, K., Surratt, J., Seinfeld, J., Ziemann, P., and Jimenez, J. (2010). Response of an aerosol mass spectrometer to organonitrates and organosulfates and implications for atmospheric chemistry. *Proceedings of the National Academy of Sciences*, 107(15):6670–6675.

[Fry et al., 2011] Fry, J., Kiendler-Scharr, A., Rollins, A., Brauers, T., Brown, S., Dorn, H.-P., Dubé, W., Fuchs, H., Mensah, A., Rohrer, F., et al. (2011). Soa from limonene: role of no 3 in its generation and degradation. *Atmospheric Chemistry and Physics*, 11(8):3879–3894.

[Fry et al., 2009] Fry, J., Kiendler-Scharr, A., Rollins, A., Wooldridge, P., Brown, S., Fuchs, H., Dubé, W., Mensah, A., Maso, M. d., Tillmann, R., et al. (2009). Organic nitrate and secondary organic aerosol yield from no 3 oxidation of β-pinene evaluated using a gas-phase kinetics/aerosol partitioning model. *Atmospheric Chemistry and Physics*, 9(4):1431–1449.

[Goldstein and Galbally, 2007] Goldstein, A. H. and Galbally, I. E. (2007). Known and unexplored organic constituents in the earth's atmosphere.

[Gross, 2004] Gross, J. H. (2004). A textbook. *SpringerVerlag Berlin Heidelberg*.

[Guenther et al., 2012] Guenther, A., Jiang, X., Heald, C., Sakulyanontvittaya, T., Duhl, T., Emmons, L., and Wang, X. (2012). The model of emissions of gases and aerosols from nature version 2.1 (megan2. 1): an extended and updated framework for modeling biogenic emissions. *Geoscientific Model Development*, 5(6):1471–1492.

[Hallquist et al., 2009] Hallquist, M., Wenger, J. C., Baltensperger, U., Rudich, Y., Simpson, D., Claeys, M., Dommen, J., Donahue, N., George, C., Goldstein, A., et al. (2009). The formation, properties and impact of secondary organic aerosol: current and emerging issues. *Atmospheric chemistry and physics*, 9(14):5155–5236.

[Hawthorne et al., 1988] Hawthorne, S. B., Miller, D. J., Barkley, R. M., and Krieger, M. S. (1988). Identification of methoxylated phenols as candidate tracers for atmospheric wood smoke pollution. *Environmental science & technology*, 22(10):1191–1196.

[Horowitz and Jacob, 1999] Horowitz, L. W. and Jacob, D. J. (1999). Global impact of fossil fuel combustion on atmospheric no x. *Journal of Geophysical Research: Atmospheres*, 104(D19):23823–23840.

[Jimenez et al., 2003] Jimenez, J. L., Jayne, J. T., Shi, Q., Kolb, C. E., Worsnop, D. R., Yourshaw, I., Seinfeld, J. H., Flagan, R. C., Zhang, X., Smith, K. A., et al. (2003). Ambient aerosol sampling using the aerodyne aerosol mass spectrometer. *Journal of Geophysical Research: Atmospheres*, 108(D7).

[Kang et al., 2007] Kang, E., Root, M., Toohey, D., and Brune, W. H. (2007). Introducing the concept of potential aerosol mass (pam). *Atmospheric Chemistry and Physics*, 7(22):5727–5744.

[Kiendler-Scharr et al., 2016] Kiendler-Scharr, A., Mensah, A. A., Friese, E., Topping, D., Nemitz, E., Prévôt, A. S., Äijälä, M., Allan, J., Canonaco, F., Canagaratna, M., et al. (2016). Ubiquity of organic nitrates from nighttime chemistry in the european submicron aerosol. *Geophysical Research Letters*, 43(14):7735–7744.

[Laakso et al., 2003] Laakso, L., Hussein, T., Aarnio, P., Komppula, M., Hiltunen, V., Viisanen, Y., and Kulmala, M. (2003). Diurnal and annual characteristics of particle mass and number concentrations in urban, rural and arctic environments in finland. *Atmospheric Environment*, 37(19):2629–2641.

[Lauraguais et al., 2016] Lauraguais, A., El Zein, A., Coeur, C., Obeid, E., Cassez, A., Rayez, M.-T., and Rayez, J.-C. (2016). Kinetic study of the gas-phase reactions of nitrate radicals with methoxyphenol compounds: experimental and theoretical approaches. *The Journal of Physical Chemistry A*, 120(17):2691–2699.

[Lee et al., 2016] Lee, B. H., Mohr, C., Lopez-Hilfiker, F. D., Lutz, A., Hallquist, M., Lee, L., Romer, P., Cohen, R. C., Iyer, S., Kurtén, T., et al. (2016). Highly functionalized organic nitrates in the southeast united states: Contribution to secondary organic aerosol and reactive nitrogen budgets. *Proceedings of the National Academy of Sciences*, 113(6):1516–1521.

[Lee et al., 2017] Lee, H.-H., Bar-Or, R. Z., and Wang, C. (2017). Biomass burning aerosols and the low-visibility events in southeast asia. *Atmospheric Chemistry and Physics*, 17(2):965–980.

[Lelieveld et al., 2015] Lelieveld, J., Evans, J. S., Fnais, M., Giannadaki, D., and Pozzer, A. (2015). The contribution of outdoor air pollution sources to premature mortality on a global scale. *Nature*, 525(7569):367.

[Li and Hou, 2003] Li, C.-S. and Hou, P.-A. (2003). Bioaerosol characteristics in hospital clean rooms. *Science of the Total Environment*, 305(1-3):169–176.

[Linstrom and Mallard, 2001] Linstrom, P. J. and Mallard, W. G. (2001). The nist chemistry webbook: A chemical data resource on the internet. *Journal of Chemical & Engineering Data*, 46(5):1059–1063.

[Liu et al., 2019] Liu, C., Liu, J., Liu, Y., Chen, T., and He, H. (2019). Secondary organic aerosol formation from the oh-initiated oxidation of guaiacol under different experimental conditions. *Atmospheric Environment*, 207:30–37.

[Liu et al., 2007] Liu, P. S., Deng, R., Smith, K. A., Williams, L. R., Jayne, J. T., Canagaratna, M. R., Moore, K., Onasch, T. B., Worsnop, D. R., and Deshler, T. (2007). Transmission efficiency of an aerodynamic focusing lens system: Comparison of model calculations and laboratory measurements for the aerodyne aerosol mass spectrometer. *Aerosol Science and Technology*, 41(8):721–733.

[Lohmann and Feichter, 2005] Lohmann, U. and Feichter, J. (2005). Global indirect aerosol effects: a review. *Atmospheric Chemistry and Physics*, 5(3):715–737.

[Middlebrook et al., 2012] Middlebrook, A. M., Bahreini, R., Jimenez, J. L., and Canagaratna, M. R. (2012). Evaluation of composition-dependent collection efficiencies for the aerodyne aerosol mass spectrometer using field data. *Aerosol Science and Technology*, 46(3):258–271.

[Mönkkönen et al., 2004] Mönkkönen, P., Uma, R., Srinivasan, D., Koponen, I., Lehtinen, K., Hämeri, K., Suresh, R., Sharma, V., and Kulmala, M. (2004). Relationship and variations of aerosol number and pm10 mass concentrations in a highly polluted urban environmentânew delhi, india. *Atmospheric Environment*, 38(3):425–433.

[Nah et al., 2015] Nah, T., Sanchez, J., Boyd, C. M., and Ng, N. L. (2015). Photochemical aging of α-pinene and β-pinene secondary organic aerosol formed from nitrate radical oxidation. *Environmental science & technology*, 50(1):222–231.

[Ng et al., 2011] Ng, N. L., Herndon, S. C., Trimborn, A., Canagaratna, M. R., Croteau, P., Onasch, T. B., Sueper, D., Worsnop, D. R., Zhang, Q., Sun, Y., et al. (2011). An aerosol chemical speciation monitor (acsm) for routine monitoring of the composition and mass concentrations of ambient aerosol. *Aerosol Science and Technology*, 45(7):780–794.

[Phan et al., 2013] Phan, N.-T., Kim, K.-H., Shon, Z.-H., Jeon, E.-C., Jung, K., and Kim, N.-J. (2013). Analysis of ammonia variation in the urban atmosphere. *Atmospheric environment*, 65:177–185.

[Pöschl, 2005] Pöschl, U. (2005). Atmospheric aerosols: composition, transformation, climate and health effects. *Angewandte Chemie International Edition*, 44(46):7520–7540.

[Ravindra et al., 2008] Ravindra, K., Sokhi, R., and Van Grieken, R. (2008). Atmospheric polycyclic aromatic hydrocarbons: source attribution, emission factors and regulation. *Atmospheric Environment*, 42(13):2895–2921.

[Rinne et al., 2009] Rinne, J., Bäck, J., and Hakola, H. (2009). Biogenic volatile organic compound emissions from the eurasian taiga: current knowledge and future directions.

[Russell et al., 1999] Russell, P. B., Hobbs, P. V., and Stowe, L. L. (1999). Aerosol properties and radiative effects in the united states east coast haze plume: An overview of the tropospheric aerosol radiative forcing observational experiment (tarfox). *Journal of Geophysical Research: Atmospheres*, 104(D2):2213–2222.

[Seinfeld and Pandis, 2016] Seinfeld, J. H. and Pandis, S. N. (2016). *Atmospheric chemistry and physics: from air pollution to climate change*. John Wiley & Sons.

[Simoneit et al., 1993] Simoneit, B. R., Rogge, W., Mazurek, M., Standley, L., Hildemann, L., and Cass, G. (1993). Lignin pyrolysis products, lignans, and resin acids as specific tracers of plant classes in emissions from biomass combustion. *Environmental science & technology*, 27(12):2533–2541.

[Sindelarova et al., 2014] Sindelarova, K., Granier, C., Bouarar, I., Guenther, A., Tilmes, S., Stavrakou, T., Müller, J.-F., Kuhn, U., Stefani, P., and Knorr, W. (2014). Global data set of biogenic voc emissions calculated by the megan model over the last 30 years. *Atmospheric Chemistry and Physics*, 14(17):9317–9341.

[Spracklen et al., 2011] Spracklen, D., Jimenez, J., Carslaw, K., Worsnop, D., Evans, M., Mann, G., Zhang, Q., Canagaratna, M., Allan, J., Coe, H., et al. (2011). Aerosol mass spectrometer constraint on the global secondary organic aerosol budget. *Atmospheric Chemistry and Physics*, 11(23):12109–12136.

[Sueper and collaborators,] Sueper, D. and collaborators. *ToF-AMS Data Analysis Software Webpage*. http://cires1.colorado.edu/jimenez-group/wiki/index.php/ToF-AMS_Analysis_Software(accessed October 10, 2019).

[Tavakoli and Olfert, 2013] Tavakoli, F. and Olfert, J. (2013). An instrument for the classification of aerosols by particle relaxation time: theoretical models of the aerodynamic aerosol classifier. *Aerosol Science and Technology*, 47(8):916–926.

[Theloke and Friedrich, 2007] Theloke, J. and Friedrich, R. (2007). Compilation of a database on the composition of anthropogenic voc emissions for atmospheric modeling in europe. *Atmospheric Environment*, 41(19):4148–4160.

[Wainman et al., 2000] Wainman, T., Zhang, J., Weschler, C. J., and Lioy, P. J. (2000). Ozone and limonene in indoor air: a source of submicron particle exposure. *Environmental Health Perspectives*, 108(12):1139–1145.

[Warner et al., 2017] Warner, J., Dickerson, R., Wei, Z., Strow, L., Wang, Y., and Liang, Q. (2017). Increased atmospheric ammonia over the world's major agricultural areas detected from space. *Geophysical research letters*, 44(6):2875–2884.

[Winer et al., 1984] Winer, A. M., Atkinson, R., and Pitts, J. N. (1984). Gaseous nitrate radical: possible nighttime atmospheric sink for biogenic organic compounds. *Science*, 224(4645):156–159.

[Wuebbles and Jain, 2001] Wuebbles, D. J. and Jain, A. K. (2001). Concerns about climate change and the role of fossil fuel use. *Fuel Processing Technology*, 71(1-3):99–119.

[Zare et al., 2003] Zare, R. N., Fernandez, F. M., and Kimmel, J. R. (2003). Hadamard transform time-of-flight mass spectrometry: more signal, more of the time. *Angewandte Chemie International Edition*, 42(1):30–35.

[Zein et al., 2015] Zein, A. E., Coeur, C., Obeid, E., Lauraguais, A., and Fagniez, T. (2015). Reaction kinetics of catechol (1, 2-benzenediol) and guaiacol (2-methoxyphenol) with ozone. *The Journal of Physical Chemistry A*, 119(26):6759–6765.

[Zhou and Wenger, 2013] Zhou, S. and Wenger, J. C. (2013). Kinetics and products of the gas-phase reactions of acenaphthylene with hydroxyl radicals, nitrate radicals and ozone. *Atmospheric environment*, 75:103–112.